Journal of Geophysical Research: Solid Earth

RESEARCH ARTICLE
10.1029/2017JB015387

Interseismic Strain Accumulation on Faults Beneath Los Angeles, California

Chris Rollins[1,2], Jean-Philippe Avouac[1], Walter Landry[3], Donald F. Argus[4], and Sylvain Barbot[5]

[1]Division of Geological and Planetary Sciences, California Institute of Technology, Pasadena, CA, USA, [2]Now at Geophysical Institute, University of Alaska Fairbanks, Fairbanks, AK, USA, [3]Walter Burke Institute for Theoretical Physics, California Institute of Technology, Pasadena, CA, USA, [4]NASA Jet Propulsion Laboratory, California Institute of Technology, Pasadena, CA, USA, [5]Earth Observatory of Singapore, Nanyang Technological University, Singapore

Key Points:
- We build GPS-based models of strain accumulation on faults beneath Los Angeles that incorporate the effect of the sedimentary basin
- We infer that three major thrust faults slip at 3-4 mm/year over the long term and are partially or fully locked on their upper sections
- This locking corresponds to a total seismic moment deficit rate of 1.6 + 1.3/-0.5 times 10^{17} Nm/year, which is presumably released in earthquakes

Supporting Information:
- Supporting Information S1

Correspondence to:
C. Rollins,
john.c.rollins@gmail.com

Citation:
Rollins, C., Avouac, J.-P., Landry, W., Argus, D. F., & Barbot, S. (2018). Interseismic strain accumulation on faults beneath Los Angeles, California. *Journal of Geophysical Research: Solid Earth*, *123*, 7126–7150. https://doi.org/10.1029/2017JB015387

Received 22 DEC 2017
Accepted 9 JUL 2018
Accepted article online 16 JUL 2018
Published online 30 AUG 2018

Abstract Geodetic data show that the Los Angeles metropolitan area is undergoing 8–9 mm/year of north-south tectonic shortening associated with the Big Bend of the San Andreas Fault. This shortening has been linked to multiple damaging twentieth century thrust earthquakes as well as possible $Mw \geq 7.0$ Holocene thrust events beneath central Los Angeles. To better characterize this seismic hazard, we assess how this shortening is being accommodated by interseismic strain accumulation on subsurface faults, incorporating detailed seismology- and geology-based models of fault geometry and the low-stiffness Los Angeles sedimentary basin. We find that strain accumulation on local strike-slip faults likely contributes no more than 1–2 mm/year of the shortening. We formally invert the geodetic data for the pattern of interseismic strain accumulation on the north dipping Sierra Madre, Puente Hills, and Compton thrust faults and a master decollement. We explore the impact of the assumed material model, strain accumulation on faults to the west and east, and other model assumptions. We infer that the three faults slip at 3–4 mm/year over the long term and are currently partially or fully locked and accruing interseismic strain on their upper sections. This locking implies an annual deficit of seismic moment, $1.6 + 1.3/-0.5 \times 10^{17}$ Nm/year in total, which is presumably balanced over the long-term average by the moment released in earthquakes. The depth distribution of moment deficit accumulation rate matches that of seismicity rates in Los Angeles to first order, in part, because the models incorporate the blind nature of the Puente Hills and Compton Faults.

1. Introduction

In California, the Pacific plate moves northwest at ~50 mm/year relative to the North American plate (e.g., Kreemer et al., 2014). The San Andreas Fault generally strikes subparallel to the relative plate motion direction and accommodates the majority of the relative motion through right-lateral slip (e.g., Argus & Gordon, 2001; Lisowski et al., 1991). North of Los Angeles, however, the San Andreas makes a leftward bend and is misaligned by ~20° with the relative plate motion direction for ~200 km (Figure 1c), resulting in north-south shortening. In Los Angeles, Global Positioning System (GPS) data (Figure 1a) show ~6 mm/year of north-south shortening between the Palos Verdes peninsula and the San Gabriel Mountains or 8–9 mm/year if Santa Catalina, San Clemente, and San Nicolas Islands are included (e.g., Argus et al., 1999, 2005; Davis et al., 1989; Feigl et al., 1993; Shen et al., 1996; Walls et al., 1998; Figures 1a and 2b). Geologic, seismologic, and strain data indicate that this shortening is the principal strain in the Los Angeles region (Davis et al., 1989; Hauksson, 1990; Li, 1996; Yang & Hauksson, 2013; Zoback et al., 1987). This shortening has been linked to the damaging 1971 $Mw \sim 6.7$ San Fernando, 1987 $Mw \sim 5.9$ Whittier Narrows, and 1994 $Mw = 6.7$ Northridge thrust earthquakes (Figure 1a; e.g., Argus et al., 1999; Dolan et al., 1995). Paleoseismologic studies suggest that it may also have produced $Mw \geq 7.0$ Holocene earthquakes on three extensive north dipping thrust faults, the Sierra Madre, Puente Hills, and Compton faults (Leon et al., 2007, 2009; Rubin et al., 1998; Figure 3). In this study, we characterize the seismic hazard associated with this shortening by using a refined GPS velocity field and detailed 3-D representations of fault geometry and subsurface elastic structure to build models of interseismic strain accumulation beneath Los Angeles. Following the preparation of various components of the modeling effort and some insights from forward models of dip-slip and strike-slip faulting, we formally invert the GPS data to estimate the long-term slip rates and the pattern of interseismic strain accumulation on the Sierra Madre, Puente Hills, and Compton faults and a master decollement. We then vet these

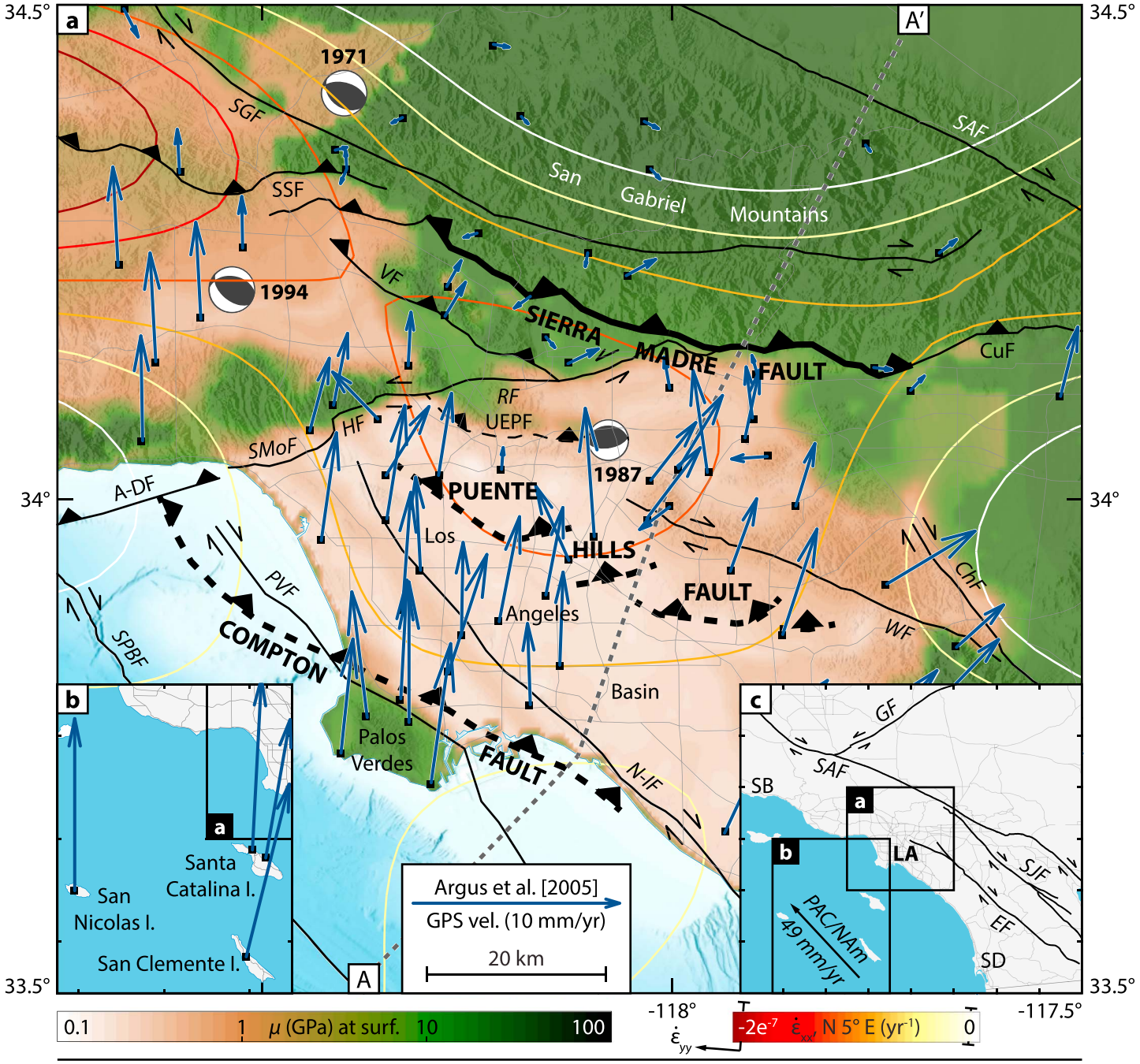

Figure 1. (a) Tectonics and shortening in the Los Angeles region. Dark blue arrows are shortening-related GPS velocities relative to the San Gabriel Mountains (Argus et al., 2005). Contours are uniaxial strain rate (rate of change of ε_{xx}) in the N ~5° E direction estimated from the GPS using the method of Tape et al. (2009). Background shading is the shear modulus at 100-m depth in the CVM*, a heterogeneous elastic model based on the Community Velocity Model (Süss & Shaw, 2003; Shaw et al., 2015) that we create and use in this study (section 4). Black lines are upper edges of faults, dashed for blind faults. Epicenters of the 1971, 1987, and 1994 earthquakes are from Southern California Earthquake Data Center; focal mechanisms are from Heaton (1982) for 1971 and Global CMT Catalog for 1987 and 1994. Profile A-A′ follows LARSE line 1 (Fuis et al., 2001) onshore and line M-M′ of Sorlien et al. (2013) offshore. SGF = San Gabriel Fault; SSF = Santa Susana Fault. VF = Verdugo Fault. SAF = San Andreas Fault. CuF = Cucamonga Fault. A-DF = Anacapa-Dume Fault. SMoF = Santa Monica Fault. HF = Hollywood Fault. RF = Raymond Fault. UEPF = Upper Elysian Park Fault. ChF = Chino Fault. WF = Whittier Fault. N-IF = Newport-Inglewood Fault. PVF = Palos Verdes Fault. (b) GPS velocities on islands. (c) Tectonic setting. Black lines and pairs of half-arrows, respectively, are major faults and their slip senses. Black arrow is Pacific Plate velocity relative to North American plate from Kreemer et al. (2014). GF = Garlock Fault. SJF = San Jacinto Fault. EF = Elsinore Fault. SB = Santa Barbara. LA = Los Angeles. SD = San Diego.

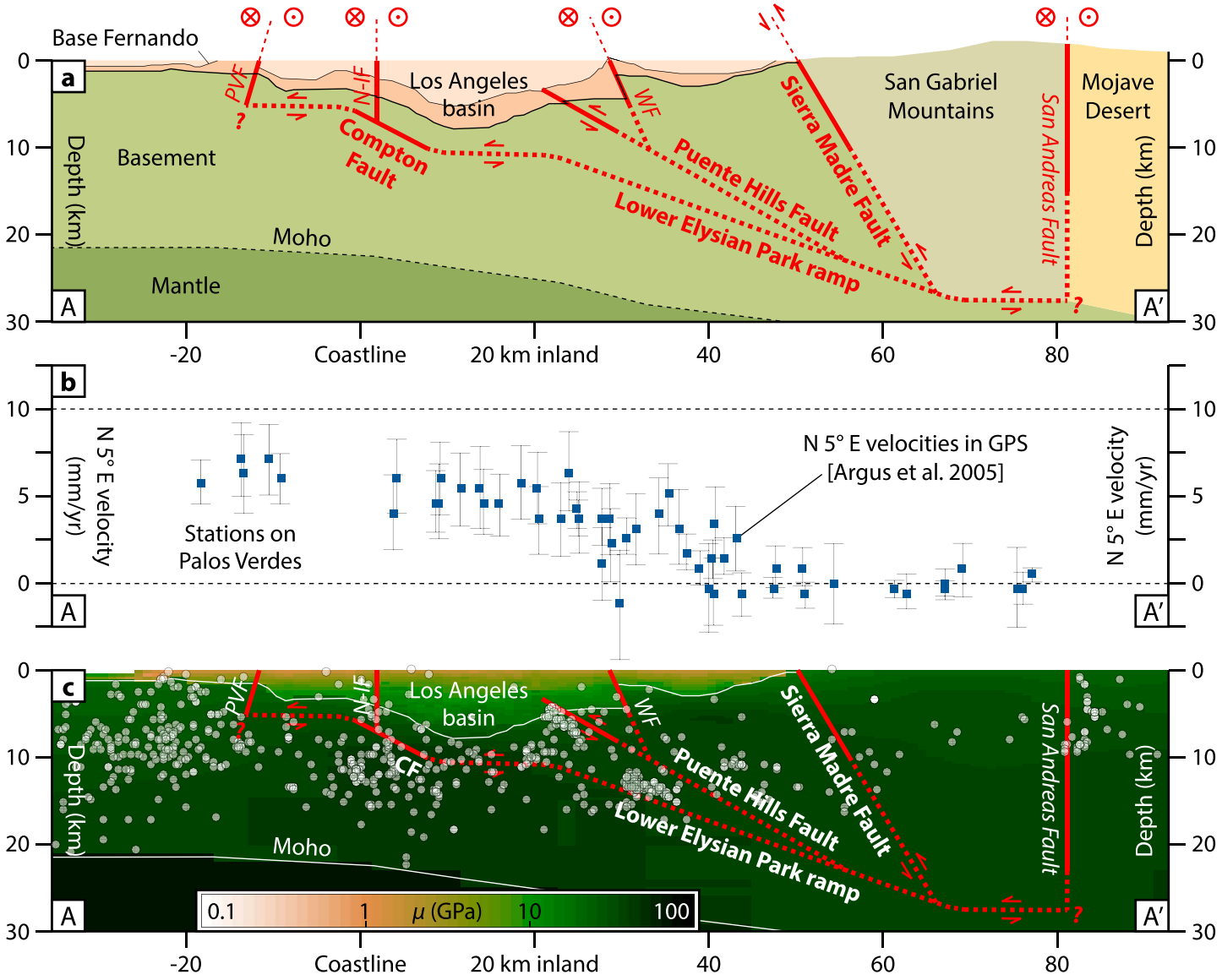

Figure 2. (a) Cross sections of faults, structure, north-south contraction, and seismicity along profile A-A′. Red lines are fault surfaces as meshed here (Figure 3), dashed where uncertain (Shaw & Suppe, 1996; Shaw & Shearer, 1999; Fuis et al., 2012). Geometries of basin, basement, and mantle are from Shaw et al. (2015); geometry of base of Fernando Formation (boundary between beige and tan units of the basin) is interpolated from Sorlien et al. (2013; offshore), Wright (1991; coastline to Whittier Fault), and Yeats (2004; Whittier Fault to Sierra Madre Fault); topography is from Fuis et al. (2012). (b) Projections of Argus et al. (2005) GPS velocities (relative to San Gabriel Mountains) onto the direction N 5° E and 1σ uncertainties. Note that stations on Palos Verdes are plotted left of the coastline as the offshore section of profile A-A′ passes alongside Palos Verdes (Figure 1a). (c) Seismotectonic features. Distribution of shear modulus is from the CVM*, the heterogeneous elastic model used in this study (section 4). Translucent white circles are relocated 1981–2016 $M \geq 2$ earthquakes whose epicenters lie within the mesh area of the three thrust faults and decollement (Hauksson et al., 2012 and updated). PVF = Palos Verdes Fault; N-IF = Newport-Inglewood Fault; WF = Whittier Fault.

models of strain accumulation by comparing them with the depth distribution of seismicity in the Los Angeles region, published geologic and paleoseismologic slip rates, and other constraints from the literature.

2. Tectonics, Geology, and Geodetic Constraints

While the Sierra Madre Fault breaks the surface along the southern edge of the San Gabriel Mountains, the Puente Hills and Compton are blind thrust faults, with top edges respectively at ~3- and ~5-km depths directly beneath the Los Angeles metropolitan area (Figures 1a and 2a). Seismic reflection data,

earthquake hypocenters, and geologic constraints suggest that the Sierra Madre and Puente Hills faults root into a decollement beneath the San Gabriel Mountains (Fuis et al., 2001; Hadley & Kanamori, 1978; Meigs et al., 2003; Myers et al., 2003; Ryberg & Fuis, 1998). This decollement may continue southward (Davis et al., 1989; Humphreys & Hager, 1990; Wright, 1991) and connect to the north dipping Lower Elysian Park ramp (Cooke & Marshall, 2006; Marshall et al., 2009; Sorlien et al., 2013). The latter likely extends upward to 10- to 11-km depth beneath central Los Angeles and may connect to the Compton Fault in a ramp-flat-ramp geometry (Shaw & Suppe, 1996), which would make the three faults a connected fold-and-thrust belt (e.g., Davis et al., 1989; Figure 2a).

Although these three north dipping thrust faults are well oriented to accommodate north-south shortening and evidently have produced $Mw \geq 7.0$ Holocene earthquakes, geologic and paleoseismologic studies provide mixed evidence about how much of the total shortening they accommodate. On the one hand, the San Gabriel Mountains are likely underlain by a crustal root whose dimensions imply that north dipping thrust faults collectively accommodate ~7 mm/year of shortening and thickening (Godfrey et al., 2002). A 1 mm/year exhumation rate inferred in the San Gabriel Mountains (Blythe et al., 2000) also suggests a total shortening rate of ~5.5 mm/year under considerations of isostasy (Donnellan et al., 2001; Meigs et al., 2003). Meigs et al. (2003) also inferred a geologic offset rate of 3.6–5.7 mm/year on the Sierra Madre Fault. However, most other geologic and paleoseismologic estimates of slip rates on the three faults, including other estimates on the Sierra Madre, are around ~1 mm/year (Bergen et al., 2017; Shaw et al., 2002 ; Shaw & Suppe, 1996; Tucker & Dolan, 2001; Walls et al., 1998) or ~2 mm/year at the maximum (Leon et al., 2007, 2009). Thus, although Argus et al. (2005) fit the geodetic shortening to a model of a north dipping edge dislocation accumulating strain at 9 ± 2 mm/year beneath northern Los Angeles and Meade and Hager (2005a) fit the shortening to interseismic strain accumulation on two north dipping faults slipping at ~4 mm/year each, these geologic and paleoseismologic slip rates suggest that deformation is more distributed. Walls et al. (1998) postulated that more than half of the shortening could be accommodated by escape tectonics on local strike-slip faults such as the right-lateral Palos Verdes, Newport-Inglewood, and Whittier faults and the left-lateral Raymond-Hollywood-Santa Monica fault system (Figure 1a); Argus et al. (1999), however, found that this model overpredicts relative east-west surface velocities in Los Angeles. Nevertheless, Marshall et al. (2009) and Daout et al. (2016) fit the geodetically inferred shortening to models of strain accumulation on thrust and strike-slip faults with slip rates closer to the geologic rates. Although the former model predicts a somewhat more gradual contractional gradient than that seen in GPS velocities, and the latter model fits only the northern portion of the shortening projected into the San Andreas-perpendicular direction (N ~25° E) rather than the north-south direction, these studies suggest that the geodetic shortening and the geologic slip rates may be reconcilable within more complex models of strain accumulation.

These studies, however, reveal another discrepancy: in the Argus et al. (2005), Marshall et al. (2009), and Daout et al. (2016) models, the best fitting locking depths on the faults accruing strain—above which they are inferred to be locked and accumulating interseismic strain as part of the cycle of stick-slip behavior and below which they are inferred to be freely creeping—are only 6 ± 2, 8, and 3 km, respectively. If true, the low-inferred strain accumulation below these depths should presumably be reflected in low seismicity rates; however, most seismicity in Los Angeles in fact occurs below these depths (Figure 2c). This discrepancy may somewhat result from the fact that these studies model the Earth as a homogeneous elastic half-space. In reality, Los Angeles sits atop a deep sedimentary basin ringed by batholithic crustal rocks (e.g., Shaw et al., 2015), a heterogeneity that may significantly affect the relationship between subsurface strain accumulation and surface deformation. In particular, the Puente Hills and Compton faults mostly underlie the Los Angeles basin (Figure 2a), and previous studies have shown that if a fault lies below a low-stiffness near-surface layer, an analysis using a homogeneous elastic model will infer slip on the fault as being shallower than it actually is (Arnadottir & Segall, 1991; Bernard et al., 1997; Cattin et al., 1999; Hager et al., 1999). The models we develop in this study incorporate this consideration.

3. The Geodetic Shortening

Geodetic strain in the Los Angeles area can result from (1) local tectonic strain accumulation, (2) deformation due to management of aquifers and oil fields, and (3) regional scale strain accumulation on the San Andreas system. Although we are only interested in the first term, the second and third must be characterized and

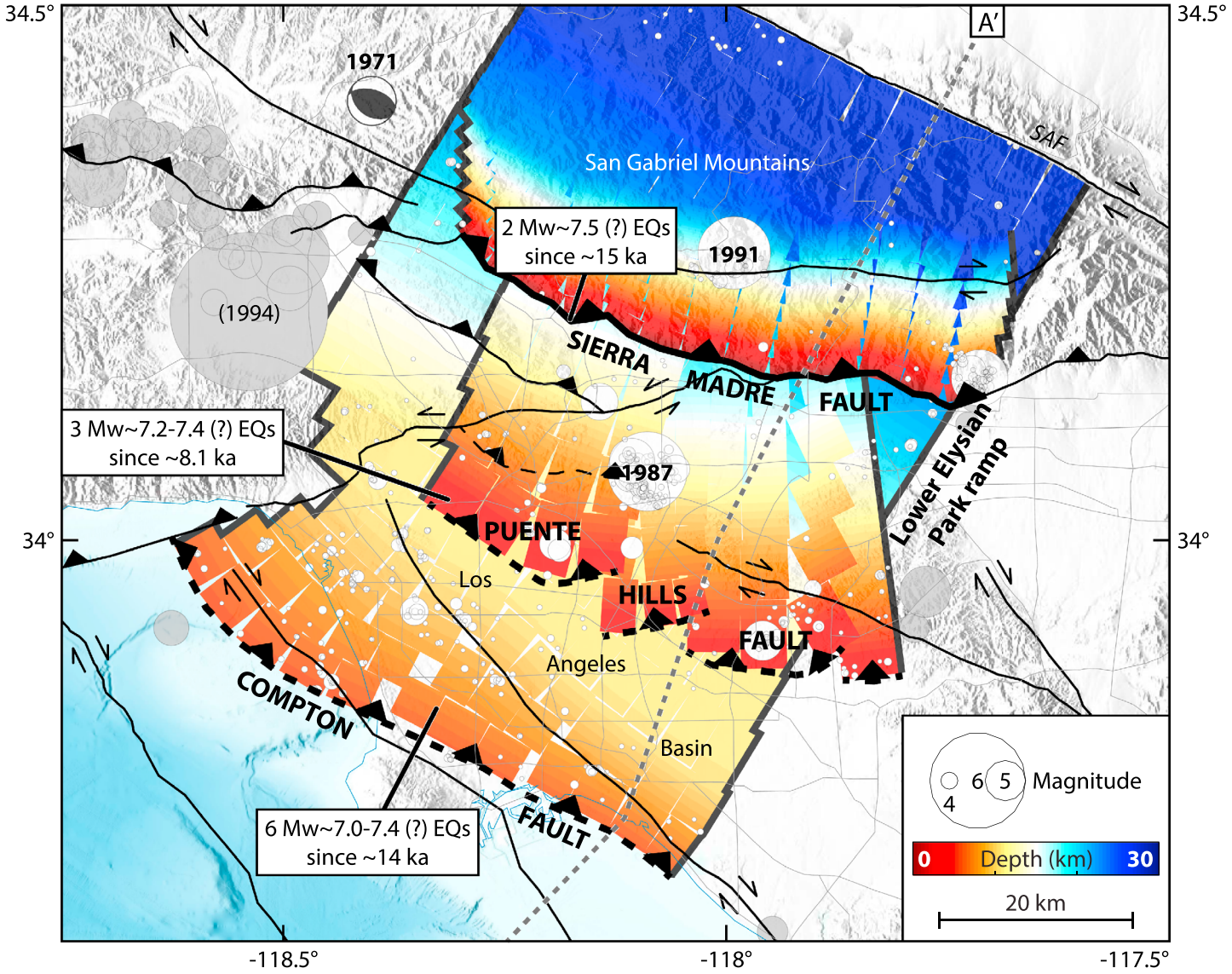

Figure 3. Meshed geometries of the three main thrust faults beneath the Los Angeles basin (section 4), colored by depth, and 1981–2016 $M \geq 2.5$ earthquakes within the mesh area from Hauksson et al. (2012 and updated), scaled by magnitude (white-filled circles). Gray-filled circles are 1981–2016 $M \geq 4.5$ earthquakes outside the mesh area. Inferred paleoearthquakes are from Rubin et al. (1998) and Leon et al. (2007, 2009). SAF = San Andreas Fault.

removed in order for a GPS data set to be of use in estimating the first. Argus et al. (2005) prepared a field of horizontal GPS velocities in Los Angeles that accounts for both anthropogenic motion (as estimated from Interferometric Synthetic Aperture Radar data) and strain accumulation on the San Andreas (as estimated using a best fit screw dislocation model). The residual velocities after subtracting both terms are expressed in the reference frame of the San Gabriel Mountains defined using a block model of long-term motion. This velocity field (Figure 1, dark blue arrows) is thus appropriate for estimating the pattern of local strain accumulation, and we use it here. Although strain accumulation on the San Andreas system is the dominant geodetic signal in southern California (e.g., Meade & Hager, 2005a), dislocation modeling shows that the inferred shortening in Los Angeles is mostly independent of the model assumed for the San Andreas (Figure S1 in the supporting information) and is therefore likely robust.

The methods we use to estimate interseismic strain accumulation on faults beneath Los Angeles (section 5) require the simultaneous estimation of present-day strain accumulation on faults and of the long-term motions across them. To reduce the number of free parameters in this approach, we assume that the

long-term shortening can be characterized as a global rotation of the Pacific Plate toward the San Gabriel Mountains block and, subsequently, that the Sierra Madre, Puente Hills, and Compton faults separate rigid intervening blocks that all move as per this global rotation at fractions of the total angular rate (fractions which the method solves for). We characterize the long-term motion of the Pacific Plate toward the San Gabriel Mountains by least squares fitting Argus et al. (2005) velocities at four stations on Santa Catalina, San Clemente, and San Nicolas Islands to a kinematic model of global rotation about an Euler pole. The pole is located at 1.42°S, 141.36°E, and the predicted rotation in Los Angeles is a near-uniform velocity field at N 4.74 ± 0.23°E at 8.5 mm/year (Figure S2), consistent with the shortening rates and azimuths inferred from geodesy, seismology, and strain orientations (e.g., Argus et al., 1999, 2005; Li, 1996; Zoback et al., 1987).

4. Faults and Elastic Structure, Elastostatic Green's Functions, and Some Inferences

The comparison of the GPS data with the predictions of a model of interseismic strain requires a set of elastostatic Green's functions that relate deformation at depth to surface displacement. This requires three elements: a representation of the deformation, a representation of the elastic medium, and a tool to the Green's functions. The deformation here (along with the plate-scale and block motions described above) is fault slip, and as details of fault geometry can affect the relationship between fault slip and surface displacement (e.g., Marshall & Morris, 2012), it is important to use accurate fault models in this estimation problem. These models are provided by the Community Fault Model, version 5 (CFM5), a component of the Unified Structural Representation (Plesch et al., 2007; Shaw et al., 2015) assembled by the Southern California Earthquake Center (SCEC). The CFM5 provides detailed 3-D geometries for dozens of faults in the Los Angeles region constrained by seismologic and geologic data. Working both from the CFM5 and an optimized variant of it (Marshall et al., 2017; Meigs et al., 2008), we construct a detailed 3-D mesh that subdivides the faults into quadrilateral patches (Figure 3), each of which will be used as the slip source in an elastostatic Green's function. The overall mesh features the Sierra Madre, Puente Hills, and Compton faults rooting into a decollement structure that includes the Lower Elysian Park ramp, thus forming a connected fold-and-thrust belt (supporting information Text S1). We also mesh the major strike-slip faults in the Los Angeles metropolitan area.

The second element is an accurate representation of the elastic medium. The Unified Structural Representation also provides the key to this in the form of the SCEC Community Velocity Model-Harvard 15.1 (CVM-H15.1), a detailed model of subsurface structure of Southern California that is also based on seismologic and geologic data and explicitly incorporates sedimentary basins (Süss & Shaw, 2003; Shaw et al., 2015). The CVM-H15.1 provides estimates of V_p, V_s, and ρ at 100-m vertical and 1-km horizontal resolution in the top 15 km of the crust and at 1-km vertical and 10-km horizontal resolution between 15- and 200-km depth. We convert the V_p, V_s, and ρ provided by the CVM-H15.1 to the Lamé parameters λ and μ using the classical seismic wave equations, $V_p = ((\lambda + 2\,\mu)/\rho)^{1/2}$ and $V_s = (\mu/\rho)^{1/2}$, yielding a detailed 3-D model of heterogeneous elastic properties that we call the CVM* (Figures 1a, 2c, and supporting information Text S2; Rollins, 2017). The contrast in V_s between the sediments of the Los Angeles basin and the batholithic rocks of much of the surrounding crust is an order of magnitude at the surface, translating into a contrast of 2 orders of magnitude in μ (Figure 1a, shaded background).

The third element is a tool that can compute elastostatic Green's functions that relate slip on the relevant faults through the elastic model to displacements at the surface. We use Gamra (Landry & Barbot, 2016), a finite-difference elastostatic modeler that solves the Navier's equation for infinitesimal strain in an arbitrarily heterogeneous medium by combining a red-black Gauss-Seidel solver, a variant of the Immersed Interface Method (Leveque & Li, 1994) to avoid numerical singularities associated with fault slip, and an adaptive meshing approach that refines the accuracy of the computation in areas of high displacement through finer sampling. We use this solver to compute elastostatic Green's functions relating slip on the subdivided patches of the quadrilateral fault mesh (Figure 3) through the CVM* to the east and north components of displacement at GPS stations. The adaptive meshing capability of Gamra allows us to compute these Green's functions at high resolution near faults and in basins without requiring high resolution in low-displacement regions (Figure S3); in particular, we compute Green's functions at 100-m vertical resolution in the Los Angeles basin, the same resolution as the CVM-H15.1 itself there.

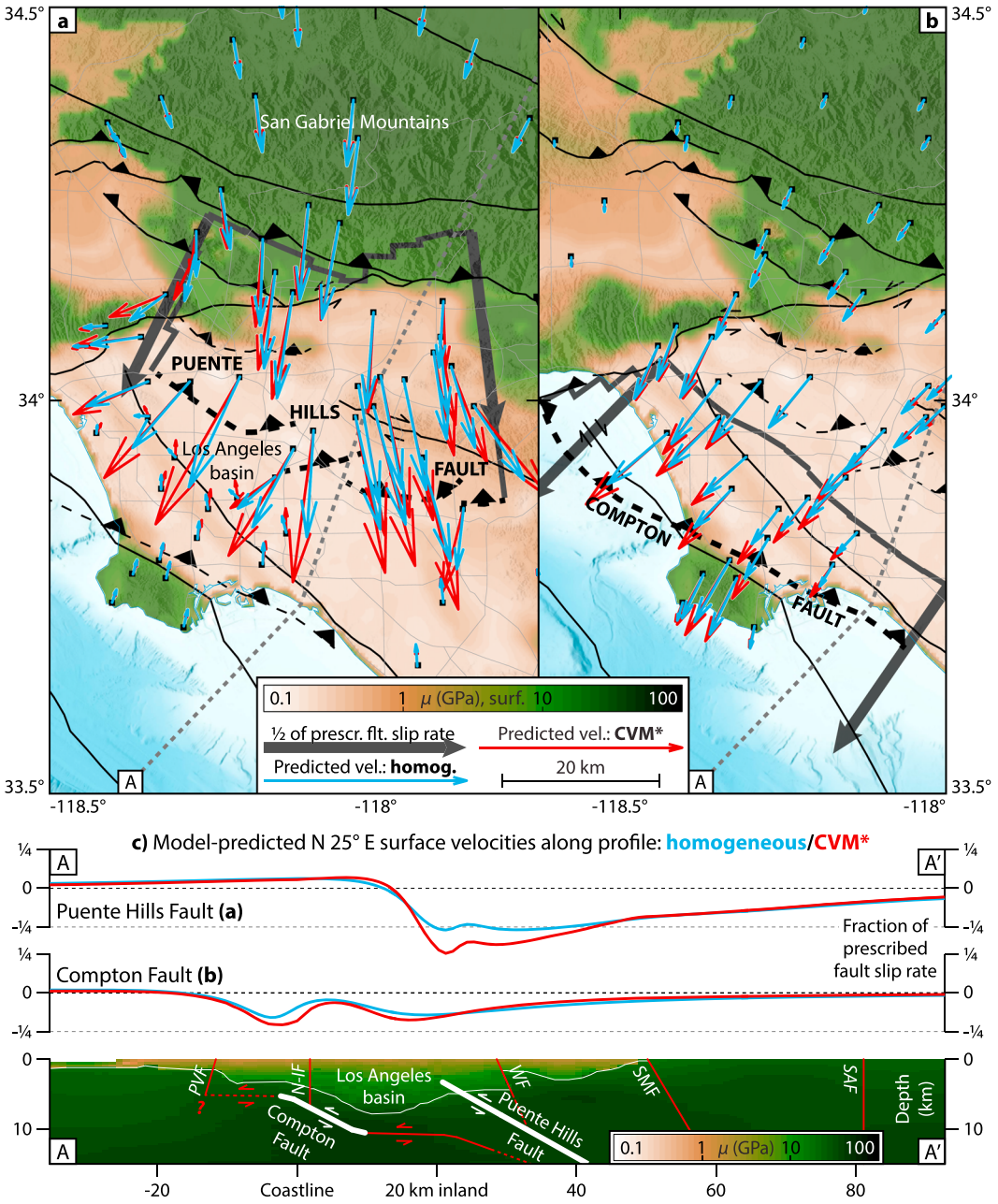

Figure 4. The Los Angeles basin amplifies elastostatic Green's functions for slip on the Puente Hills (a) and Compton (b) faults, as shown here with forward models of uniform slip on each fault. Blue and red arrows are model-predicted GPS surface velocities calculated in a homogeneous half-space model and in the CVM*, respectively. White arrows are the difference between the two. All velocities are normalized by the prescribed slip rate on the fault; large gray arrows are half of that slip rate (they show the hanging wall motion directly on the fault.) Background shading is μ at 100-m depth in the CVM*. Fault geometries are outlined in gray. (c) Model-predicted velocities (in the homogeneous half-space and the CVM*) projected into the N 25° E direction along profile A-A′ and cross section of faults and the CVM*. CPVF = Palos Verdes Fault; N-IF = Newport-Inglewood Fault; WF = Whittier Fault; SMF = Sierra Madre Fault; SAF = San Andreas Fault.

We evaluate the effect that the elastic model has on the elastostatic Green's functions by computing the predicted surface displacement field from uniform reverse slip on the Puente Hills Fault, first with a homogeneous elastic model (Okada, 1985) and then with the CVM*. A comparison of the two (Figures 4a and 4c) shows that the sediments of the Los Angeles basin amplify the surface displacements related to slip on

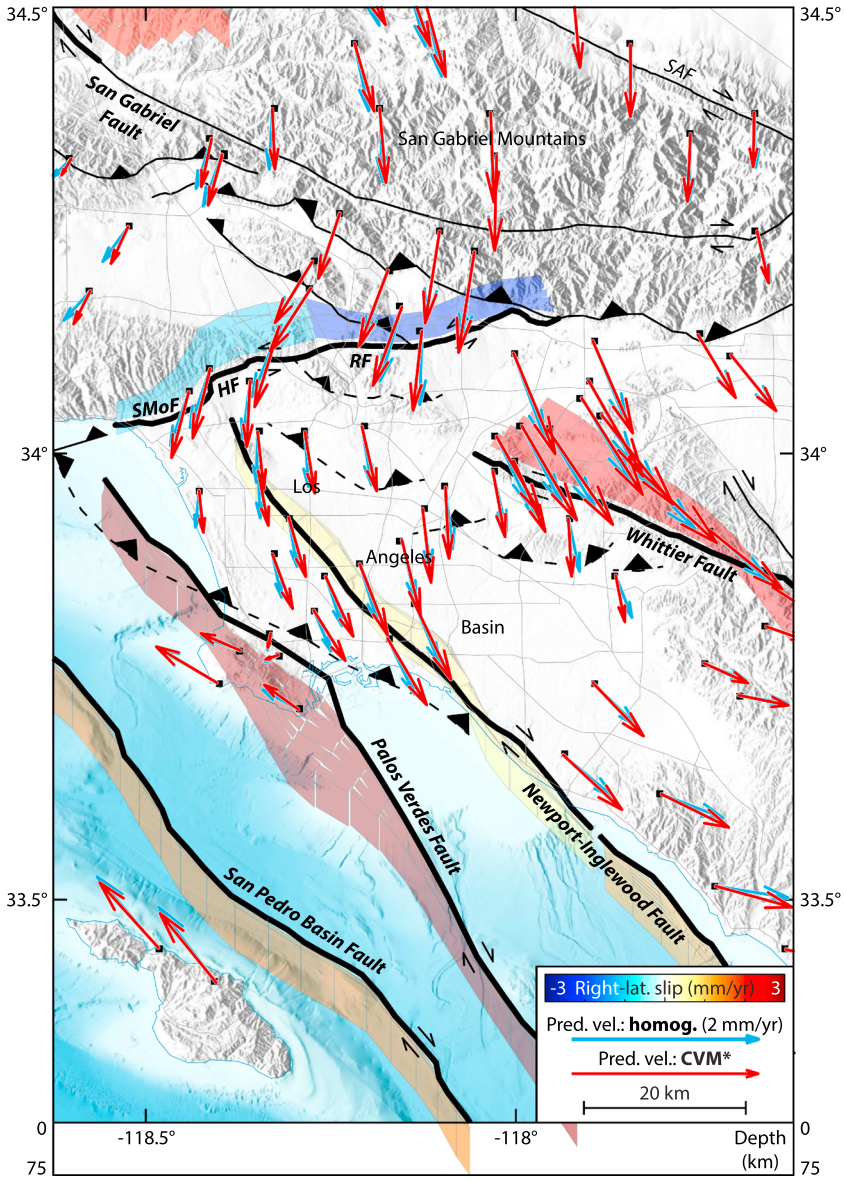

Figure 5. Strain accumulation on local strike-slip faults could contribute up to ~1.8 mm/year of north-south shortening, as shown here with a forward model in which the strike-slip faults slip at their UCERF3 consensus "Geologic" slip rates between ~5- and 75-km depths. Blue and red arrows are the predicted surface velocity fields calculated in a homogeneous half-space and in the CVM*, respectively. (Look angle is slightly northward rather than vertically down; San Pedro Basin Fault, Palos Verdes Fault and southern Newport-Inglewood Fault all dip vertically.) SAF = San Andreas Fault; SMoF = Santa Monica Fault; HF = Hollywood Fault. RF = Raymond Fault.

the underlying Puente Hills Fault by up to 50% compared to the homogeneous model. The Green's functions appear to be insensitive to local details of the CVM* (Figure S4 and supporting information Text S2) and are controlled more by the overall contrast in elastic moduli between the basin sediments and surrounding crust. The basin also amplifies elastostatic Green's functions for slip on the underlying Compton Fault (Figures 4b and 4c). The uppermost Sierra Madre Fault cuts through low-stiffness near-surface material which, relative to a homogeneous elastic body, damps the elastostatic Green's functions for slip on this upper section and confines them closer to the fault (Figure S5). We note also, as discussed by Marshall et al. (2009), that slip on the Sierra Madre produces larger horizontal displacements in the footwall than in the hanging wall as a product of the fault's relatively steep (~55°) dip (Figure S5), suggesting that the rapid geodetic shortening between the Puente Hills and Sierra Madre Faults (Figure 2b) could be interpreted as resulting from

interseismic strain accumulation on either fault or on both. The Green's functions from slip on the Upper Elysian Park Fault, for which Oskin et al. (2000) estimate a reverse slip rate of 0.9–2.2 mm/year, are proportionally low in amplitude due to the fault's small size and shallow position (Figure S6), and we infe that the Compton, Puente Hills, and Sierra Madre faults likely play larger roles in accommodating the shortening.

We also compute elastostatic Green's functions for slip on major strike-slip faults in and around the Los Angeles basin. As the geodetic data are likely too sparse to warrant models featuring both thrust and strike-slip faults, we use these Green's functions to assess a priori how much the strike-slip faults could be contributing to the observed north-south shortening. To place an upper bound on this effect, we build a forward model in which the strike-slip faults slip at their consensus *geologic* slip rates from the Unified California Earthquake Rupture Forecast, Version 3 (Field et al., 2014) between an upper locking depth of ~5 km and a maximum depth of 75 km, the approximate depth to the lithosphere-asthenosphere boundary in Los Angeles (Lekic et al., 2011). This model (Figure 5) produces ~1.8 mm/year of north-south shortening across the Los Angeles basin with comparatively low east-west velocities, in contrast to the findings of Argus et al. (1999). A model with the strike-slip faults locked down to ~13-km depth with the same slip rates produces ~1.1 mm/year of north-south shortening (Figure S7). The limitations of these models are that (1) the total shortening is less than a quarter of the ~8.5 mm/year observed and (2) the fastest predicted shortening is around the Palos Verdes Fault (Figures 5 and S7) rather than in the northern Los Angeles basin, which is inconsistent with the GPS data (Figure 2b). This suggests that the contribution of strike-slip faults to the total shortening is second order and that it may not be oversimplifying to use only the three main thrust faults in GPS-based models of strain accumulation. (We do, however, subsequently explore the effect of accounting for the contribution of strike-slip faults a priori in models of thrust faulting.)

5. Kinematic Inversions for Interseismic Strain Accumulation on Thrust Faults

5.1. Overall Scheme

We formally invert the Argus et al. (2005) velocities at four stations on islands (Figure 1b) and 54 stations overlying the Sierra Madre, Puente Hills, and Compton faults and decollement for the pattern of interseismic strain accumulation on these faults. We use the back slip framework (Savage, 1983), which expresses the pattern of interseismic deformation on a fault as the sum of long-term steady-state deformation across the fault plus backward creep on the sections that are partially or fully locked during the interseismic period. The rate of backward creep is the rate at which a given section is lagging behind the fault's long-term slip rate during the interseismic period and thus accruing a deficit of slip that will presumably be compensated by coseismic slip in future earthquakes. We call this the slip deficit accumulation rate. Its distribution can then be multiplied by the areas of the slip patches and the shear modulus μ along them (from the CVM*) to yield the rates at which deficits of seismic moment are accruing on them, deficits which will presumably be compensated by the moment release in those future earthquakes (Brune, 1968; Molnar, 1979). Integrating this distribution over the fault system then yields the cumulative moment deficit accumulation rate on these faults during the interseismic period.

We explore two complementary inversion schemes as well as the effects of various assumptions. These schemes solve for the model $\mathbf{m}_{est}$ that minimizes the quantity $||(\mathbf{d} - \mathbf{Gm})/\boldsymbol{\sigma}||_2$ subject to regularization. Here $\mathbf{d}$ is the vector of the east and north components of GPS velocities and $\boldsymbol{\sigma}$ is the vector of their uncertainties (whose preparation is described in supporting information Text S3). The matrix $\mathbf{G}$ includes the elastostatic Green's functions, each of which maps (backward) slip on a subdivided patch of the thrust fault mesh (Figure 3) through the CVM* (unless otherwise specified) to the east and north components of motion at the 58 GPS stations. The corresponding output model parameters will be the estimated interseismic slip deficit accumulation rates on the fault patches.

The matrix $\mathbf{G}$ also includes four other columns. The first accounts for the background long-term rotation of the stations toward the San Gabriel Mountains (supporting information Text S4, last paragraph) and does not factor into strain. The other three describe the long-term steady state motion across each of the three faults. The corresponding three model parameters, after accounting for the dips of the faults, will be estimates of their long-term forward slip rates. We assume that the faults offset rigid blocks that are all rotating about the previously computed Euler pole, so the steady state terms are 2-D steps in the modeled global

rotation field (Figure S2, light blue arrows) across the faults' surface breaks (e.g., Ader et al., 2012; Matsu'ura et al., 1986). For the blind Puente Hills and Compton faults, we assume more specifically that the long-term deformation updip of the faults' upper edges is consistent with the overall long-term block motions but is itself anelastic over the long term and contributes negligibly to the interseismic elastic deformation pattern. This updip deformation likely occurs primarily through anelastic fault-tip folding (e.g., Allmendinger & Shaw, 2000) which may occur mainly during large earthquakes, as is assumed in paleoseismologic studies of these faults (e.g., Dolan et al., 2003; Leon et al., 2009), and therefore, its contribution to interseismic deformation may indeed be second order. We incorporate this assumption into the elastic modeling here by adding updip fault sections aligned with the surface projections of the Puente Hills and Compton faults, enforcing that those updip sections are completely locked (which in this framework is equivalent to assuming that they do not exist), adding the scaled summed elastostatic Green's functions from slip on the updip sections to the steady state terms for each fault for internal consistency and then not counting this locking in the interpretations of strain accumulation, as detailed in supporting information Text S4 (Broderick, M.S. thesis, 2006, as cited in Sorlien et al., 2013). We later evaluate the impact of this assumption by assessing how our major findings would change if the strain accumulation on the locked updip extensions of the blind faults were counted. For self-consistency, we enforce that slip on each fault patch is in the local direction of the global rotation field at that patch, so the elastostatic Green's functions in **G** are from a mixture of dip slip and strike slip depending on the orientations of the patches (unlike in the forward models previously described). Thus, all motion is in the plate-scale convergence direction.

Another factor to consider is whether strain accumulation on thrust faults west and east of the Los Angeles basin may influence the geodetic velocity field in the basin. The seismic potential of thrust faults west of the basin has been demonstrated by the 1994 Mw = 6.7 Northridge earthquake, and multiple thrust systems to the west have long-term slip rates of several millimeters per year (e.g., Dolan et al., 1995; Donnellan et al., 1993; Hager et al., 1999; Marshall et al., 2013). Fewer extensive thrust faults reside to the east of the basin (e.g., Marshall et al., 2009), as the tectonics become dominated by the San Andreas and San Jacinto Faults (which are modeled out a priori in the Argus et al. (2005) velocity field), but the Sierra Madre Fault does continue eastward as the Cucamonga Fault, which may have a reverse slip rate of several millimeters per year (Morton & Matti, 1987). We therefore leave this an open consideration, exploring models that include strain accumulation both west and east of the basin (in addition to on the three thrust faults), models that do not, and models that include it on one side but not the other (supporting information Text S4). We then let the first-order features of these models' fits to the data inform us about which configurations may provide the best representation.

We quantify each model's fit to the data using the weighted mean square error, $X^2/N = ||(\mathbf{d} - \mathbf{Gm})/\boldsymbol{\sigma}||_2/N$, where N is the length of the data vector. This quantity is similar to the reduced chi-square statistic but does not subtract the number of model parameters from N as this number is unknown for regularized models (Chlieh et al., 2008). A X^2/N value of ~0.5, as we obtain with the best fitting models described subsequently, corresponds to a mean misfit of ~0.8 mm/year on each component of velocity at each station overlying the mesh, on average ~50% lower than the Argus et al. (2005) uncertainties. The latter may be conservatively large as they (1) include each station's absolute velocity uncertainty in a global reference frame, (2) include uncertainties on the anthropogenic motions which are estimated as comparable to the anthropogenic motions themselves, and (3) do not include covariances between stations with respect to either source of uncertainty. Therefore, the low X^2/N values we obtain do not indicate overfitting.

5.2. The *Smoothed* Inversion Scheme and Model 1a

The first inversion scheme we use, called the smoothed scheme, imposes spatial smoothing on the distribution of slip deficit accumulation rate, as commonly done in models of interseismic strain accumulation (e.g., Ader et al., 2012; Bürgmann et al., 2005; Chlieh et al., 2008). This can be interpreted as an assumption that the transition from creep to locking on a fault occurs gradually in space. To reduce the effect of potential errors in the GPS velocities due to incorrect characterization of anthropogenic motions (Marshall et al., 2009) and to better address potential issues such as the possible trade-off between the Puente Hills and Sierra Madre faults due to the latter's steep dip (section 4), we use this inversion in a delete-half jackknife scheme (e.g., Tichelaar & Ruff, 1989), in which it is performed on 1,000 sets of velocities that each use half of the 58 GPS stations (with

all sets enforced to have at least one station offshore), generating 1,000 models of long-term slip rates and slip deficit accumulation rates. We subsequently describe the weighted mean distribution of slip deficit accumulation rate and weighted mean long-term slip rates from the sets of 1,000 models, where each individual model's assigned weight is the inverse exponential of its X^2/N value. Details of this scheme are provided in supporting information Text S5 (Aster et al., 2012; Barbot et al., 2013; Kositsky & Avouac, 2010; Ortega, Ph.D. thesis, 2013).

We use this scheme to invert the GPS velocity field for the long-term slip rates on the Sierra Madre, Puente Hills, and Compton faults and the distribution of slip deficit accumulation rate on the fault mesh. The first inversion allows strain accumulation both east and west of the Los Angeles basin (supporting information Text S4). This yields Model 1a of interseismic strain accumulation (Figure 6), which fits the GPS with $X^2/N = 0.49$. The model infers the fastest slip deficit accumulation rates on the shallowest sections of the faults, particularly on the upper Sierra Madre Fault (Figure 6a); however, the fastest moment deficit accumulation rates are deeper (Figure S11) due to the increase of shear modulus with depth (Figure S9). The estimated long-term slip rates on the Sierra Madre, Puente Hills, and Compton faults are, respectively, 4.6, 3.1, and 3.6 mm/year. The 1,000 jackknife models provide 1,000 measurements of the cumulative rate at which seismic moment deficit accumulates in the system. We use MATLAB's ksdensity function to construct the weighted probability density function (PDF) of moment deficit accumulation rate. The PDF peaks at 2.0×10^{17} Nm/year, its weighted mean is 2.4×10^{17} Nm/year, and its one sigma range (16th/84th percentiles) is $1.5–3.4 \times 10^{17}$ Nm/year (Figure 6b).

To test the effect that the elastic structure has on the estimation of strain accumulation, we perform the same inversion with elastostatic Green's functions from a homogeneous elastic half-space model. The resulting model (Figures 6d and S11a) features distinctly slower slip deficit accumulation rates on all three faults. The elastostatic Green's functions for slip on the upper Sierra Madre Fault are proportionally damped by the CVM* as compared to a homogeneous elastic body (Figure S5), and so less slip is required on this upper section to fit a given surface deformation pattern when using a homogeneous elastic model than when using the CVM*, likely explaining the slower slip deficit rates on the fault in this auxiliary model; a similar effect may occur on the Puente Hills and Compton Faults although complicated somewhat by their blind nature. The PDF of the cumulative moment deficit accumulation rate (computed assuming a uniform shear modulus μ = 30 GPa) peaks at 1.3×10^{17} Nm/year in this homogeneous model, with a weighted mean of 1.7×10^{17} Nm/year (Figure 6b, blue line; Figure S12b), substantially less than the rates in Model 1a. The fit to the data ($X^2/N = 0.49$) is as good as that of Model 1a, suggesting that the GPS velocity field may not itself be diagnostic of the elastic structure.

We then run auxiliary inversions to test (1) the effect that potentially erroneous GPS velocities may have on the model (Figure S13) and (2) the difference that would result from subtracting the upper bound strike-slip velocity field (Figure 5) from the data set a priori and also not using GPS velocities on islands (Figure S14). This model yields patterns of slip deficit accumulation rate that are similar to that in Model 1a (Figures S13 and S14) and respective weighted mean cumulative moment deficit accumulation rates of 2.1×10^{17} Nm/year and 2.6×10^{17} Nm/year, both only marginally different from that in Model 1a (supporting information Text S6).

5.2.1. The Role of Strain Accumulation West and East of the Basin and Model 1b

Model 1a, in addition to estimating the strain accumulation on the three thrust faults, allows interseismic strain to accumulate east and west of the Los Angeles basin. To test the impact of this assumption, we try an inversion that disallows this external strain accumulation (supporting information Texts S4 and S5). The resulting model (Figure S15) fits the data considerably less well, with $X^2/N = 0.71$, and in particular, it predicts that GPS velocities should exhibit an outward component of motion on the sides of the basin (Figure S15a). This is a signature of a laterally confined thrust dislocation, as seen in the models of uniform slip on individual faults (Figures 4a and S5). In Model 1a, by contrast, the predicted velocities exhibit no edge effects (Figure 6a), as the displacement source is much longer than the area of data coverage. The real GPS velocities show no systematic outward motion on the west side of the Los Angeles basin, suggesting that strain accumulation on faults to the west influences those velocities and is thus a necessary component of models. By virtue of confining strain accumulation to the basin, this model also substantially underpredicts GPS velocities on the islands to the southwest and west (Figure S15b), suggesting that it is also difficult to fit those velocities without invoking strain accumulation west of the basin. The *basin-only* model, however, yields a good fit to GPS

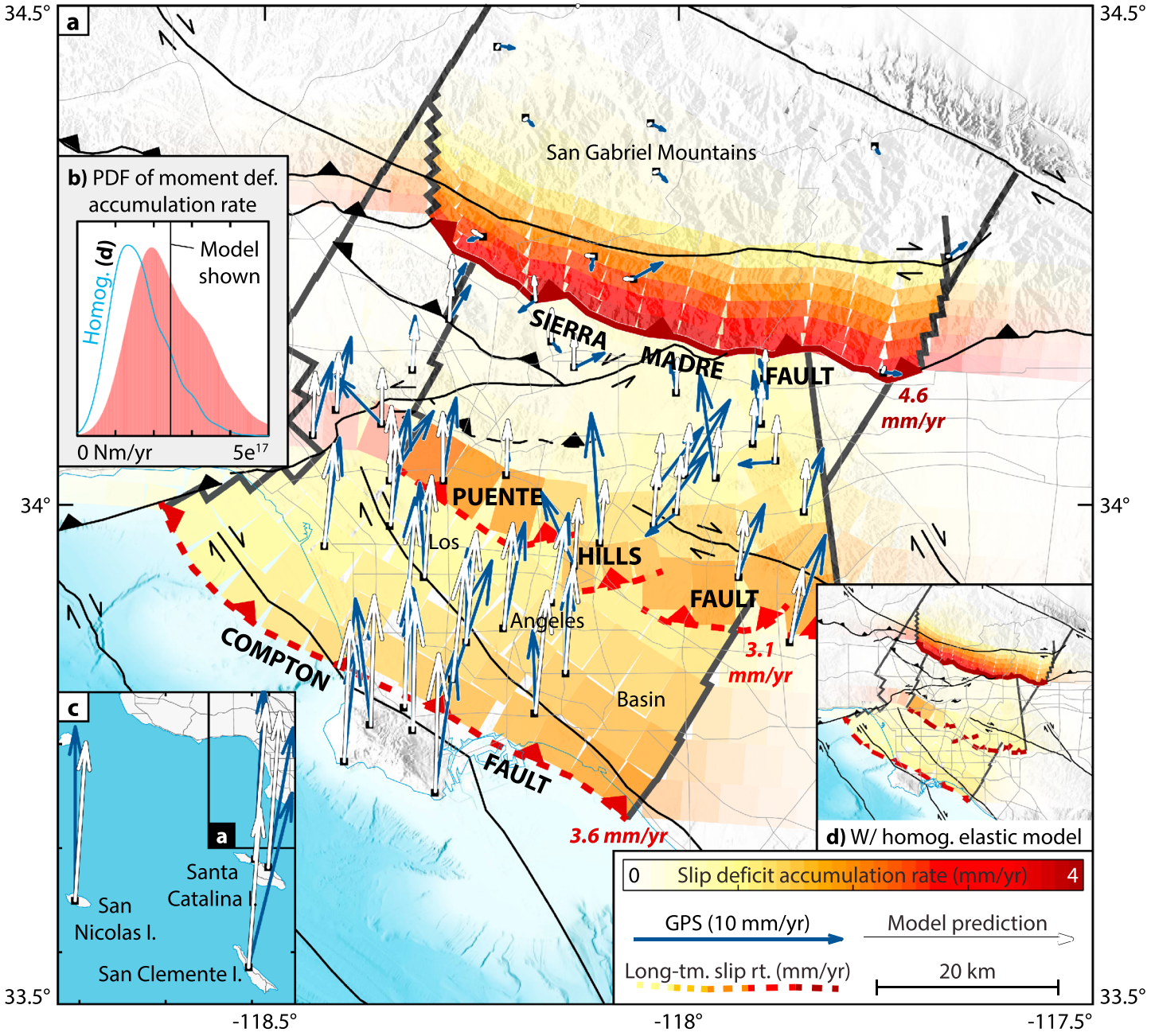

Figure 6. Model 1a of slip deficit accumulation rates and long-term slip rates on the Compton, Puente Hills, and Sierra Madre faults, using the smoothed scheme and allowing strain accumulation east and west of the basin. (a) Map view of slip deficit accumulation rates (colored patches), long-term slip rates (colors of the solid and dashed fault traces, also noted next to the faults), and observed (dark blue) and predicted (red) velocities at GPS stations. (b) Weighted PDF of moment deficit accumulation rate constructed from the 1,000 delete-half jackknife models of which the slip deficit accumulation rate distribution plotted here is the weighted average. The blue line is the PDF using a homogeneous elastic half-space assumption (Figure S12). (c) Comparison of observed and predicted velocities on islands. (d) Model computed assuming a homogeneous elastic half-space (Figure S12) for visual comparison.

velocities on the east side of the basin (Figure S15a). The case for including strain accumulation on thrust faults outside the basin in models therefore seems stronger on the west side than on the east side, both in terms of fitting the GPS data and as evidenced by geologic studies.

We therefore try an inversion that allows for strain accumulation west of the basin but not to the east (Figure 7). The resulting model, which we call Model 1b, reproduces the azimuths of GPS velocities on the east side of the basin (Figure 7a), predicts no westward rotation on the west side, and fits the velocities on islands

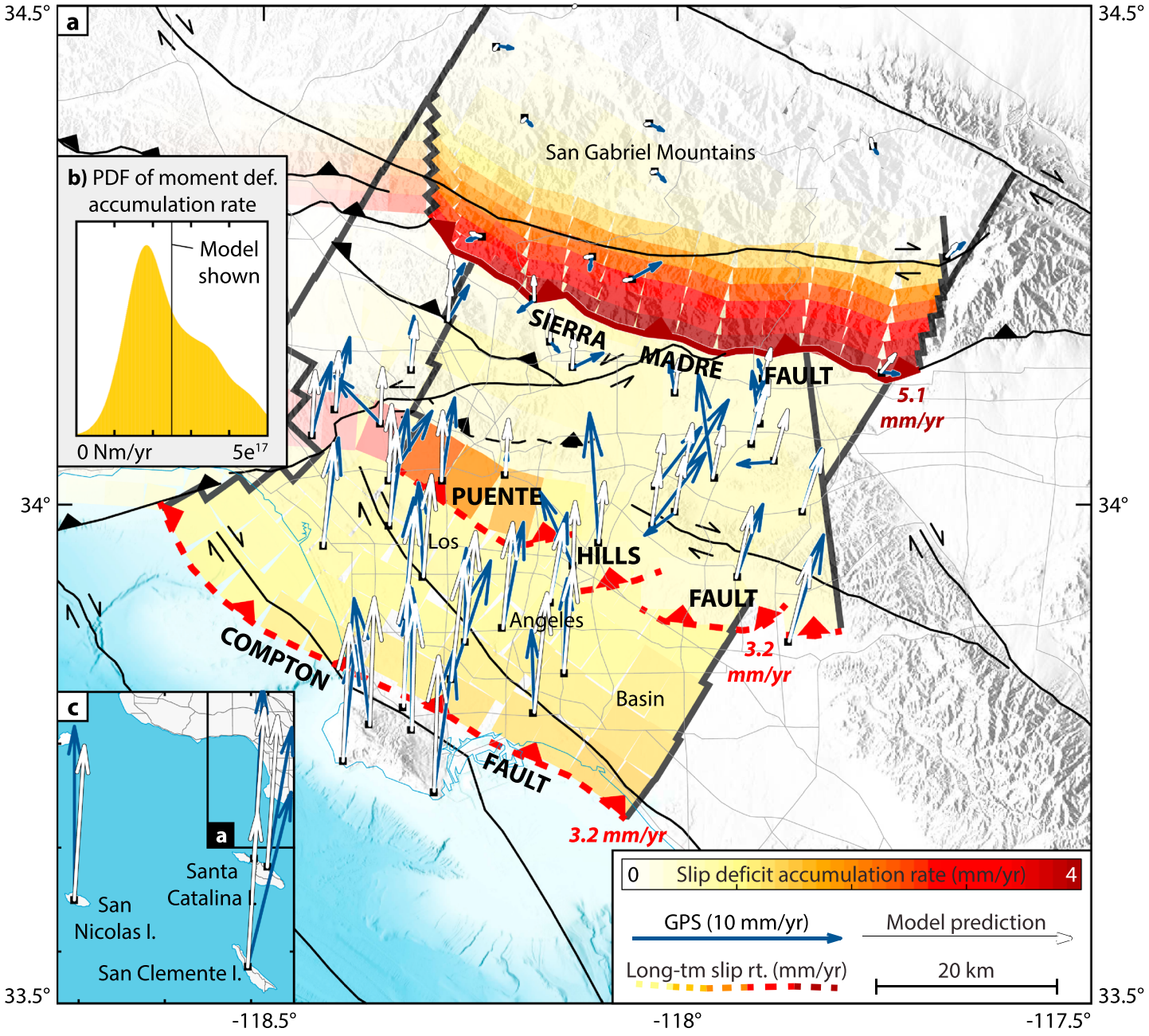

Figure 7. Model 1b of slip deficit accumulation rates and long-term slip rates, using the smoothed scheme but disallowing strain accumulation east of the basin. (a) Map view of slip deficit accumulation rates (colored patches), long-term slip rates (colors of the solid and dashed fault traces, also noted next to the faults), and observed (dark blue) and predicted (yellow) velocities at GPS stations. (b) Weighted PDF of moment deficit accumulation rate constructed from the 1,000 delete-half jackknife models of which the slip deficit accumulation rate distribution plotted here is the weighted average. (c) Comparison of observed and predicted velocities on islands.

as well as Model 1a (Figure 7c), with $X^2/N = 0.49$, an equally good overall fit. It infers long-term slip rates of 5.1, 3.2, and 3.2 mm/year on the Sierra Madre, Puente Hills, and Compton faults, respectively. Slip deficit accumulation rates are slower on the eastern Puente Hills and Compton faults than in Model 1a and faster on the eastern Sierra Madre, likely because this model disallows strain accumulation on the Cucamonga Fault to the east and hence attributes proportionally more surface shortening to strain accumulation on the Sierra Madre. The cumulative moment deficit accumulation rate is nonetheless similar to Model 1a: the PDF (Figure 7b) peaks at 1.8×10^{17} Nm/year with a one sigma range of $1.5–3.6 \times 10^{17}$ Nm/year and a weighted mean of 2.5×10^{17} Nm/year.

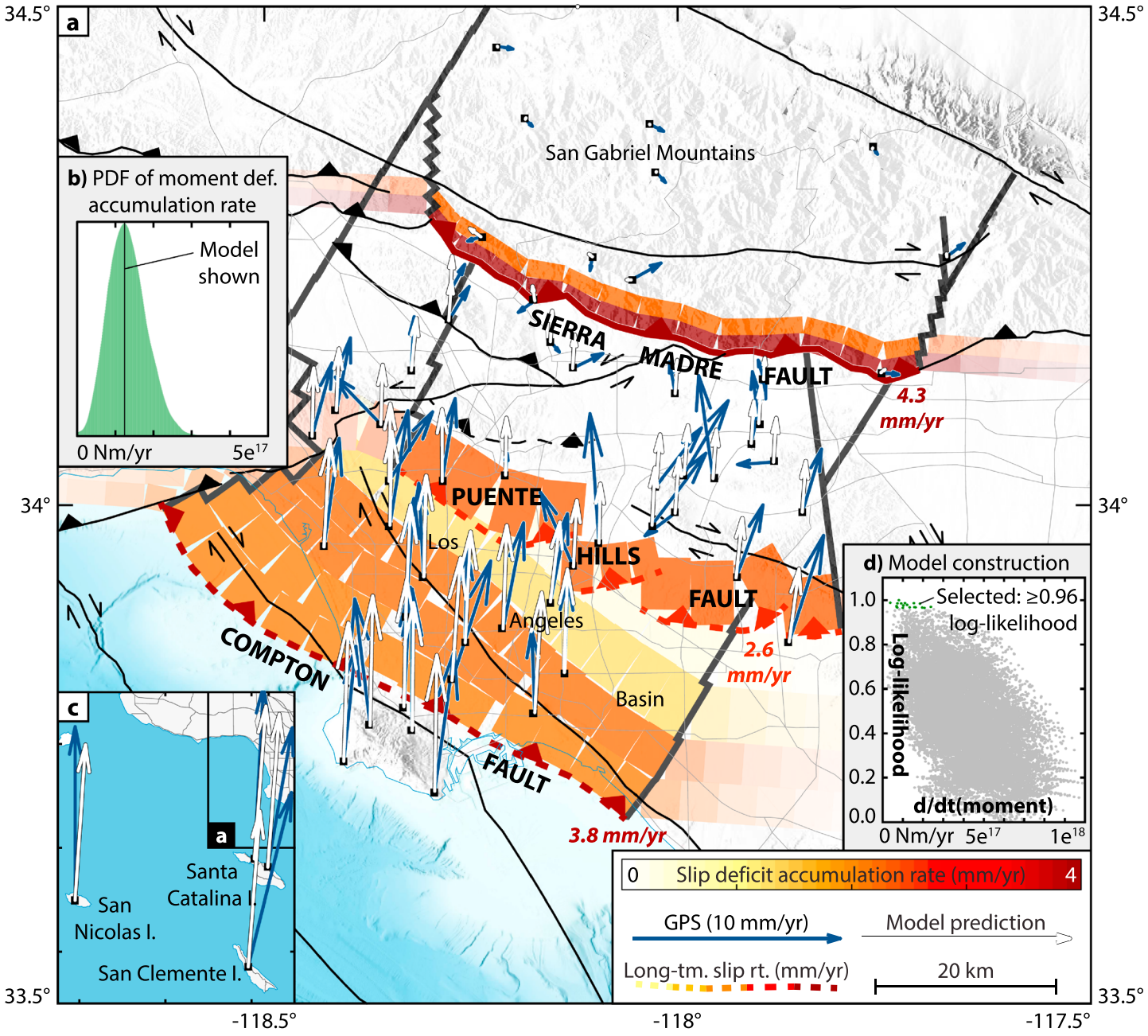

Figure 8. Model 2a of slip deficit accumulation rates and long-term slip rates, the weighted average of a set of binary creep/locking models allowing strain accumulation east and west of the basin that have normalized log likelihood ≥0.96. (a) Map view of slip deficit accumulation rates (colored patches), long-term slip rates (colors of the solid and dashed fault traces, also noted next to the faults), and observed (dark blue) and predicted (green) velocities at GPS stations. (b) Corresponding PDF of moment deficit accumulation rate (supporting information Text S8). (c) Comparison of observed and predicted velocities on islands. (d) Distribution of moment deficit accumulation rate versus normalized log likelihood in the set of binary models.

5.3. The *Binary* Inversion Scheme and Model 2a

We then wish to assess how these interpretations would change if the creep-to-locking transition on faults (and therefore the transition from relatively high to near-zero interseismic slip deficit accumulation rates) was assumed to occur sharply in space rather than gradually. To do so, we devise a second inversion scheme, hereafter called the binary scheme, where the GPS data are fit to a suite of models in which slip deficit accumulation rates are enforced to have a binary behavior with depth (e.g., Chlieh et al., 2011). In each model,

each fault is enforced to be accumulating slip deficit at its full long-term slip rate over a prescribed depth range (uniformly along strike) and freely slipping at all other depths; the inversion then solves for the best fitting long-term slip rates on the three faults (Figure S16). We then compute the slip rates and X^2/N for every combination of upper and lower locking depths on the faults. Details of this scheme are provided in supporting information Text S7.

We first run this binary scheme while allowing strain accumulation both west and east of the basin, as in Model 1a. A plot of all misfits against all upper and lower locking depths output from this approach (Figure S17) shows that all of the best fitting models feature the Sierra Madre Fault's upper locking depth at the surface and its lower locking depth below the surface, that is, a locked upper Sierra Madre Fault, as inferred in Models 1a and 1b. The best fitting models also feature the top 3 km of the Puente Hills locked, similar to Models 1a and 1b, although this has less impact on the misfit. The fit gradually deteriorates with increasing lower locking depth on the Sierra Madre and on the Compton-decollement system, echoing the smoothed models' inference of downward decreasing slip rates on those faults. The best fitting models also feature slip rates of 4–5 mm/year on the Sierra Madre, 2–3 mm/year on the Puente Hills, and ~4 mm/year on the Compton (Figure S18), consistent with Models 1a and 1b.

To then combine the binary models into a single estimate of interseismic strain accumulation, we select the 19 binary models with normalized log likelihoods of 0.96 or greater (Figure 8d, blue points) and then use the weighted mean slip deficit accumulation rate distribution, long-term slip rates, and moment accumulation rate from these models. (The cutoff value of 0.96 was chosen by inspection of models above and below it; Elliott et al., 2016, from which this method is inspired, uses 0.95.) The resulting model (Figure 8a), hereafter referred to as Model 2a, has a slightly lower misfit than Models 1a and 1b (X^2/N = 0.46) and shares some similarities to Model 1a, with respective slip rates of 4.3, 2.6, and 3.8 mm/year on the Sierra Madre, Puente Hills, and Compton faults and relatively rapid slip deficit accumulation rates on the uppermost sections of the faults. This model, however, infers no strain accumulation on the deeper sections of the faults and yields a weighted mean moment deficit accumulation rate of 1.2×10^{17} Nm/year, only 50% as fast as Models 1a and 1b. The difference arises from different treatment of these deeper sections: the *smoothed* method enforces that slip deficit accumulation rates on them should be spatially smooth but not necessarily zero, while they are zero at depth in Model 2a because none of the best fitting 19 models averaged to form it feature complete locking down to those depths. The contrast thus appears to parallel the contrast in assumptions between the smoothed and binary schemes.

We then wish to derive a PDF of moment deficit accumulation rate corresponding to Model 2a as a counterpart to the PDFs corresponding to Models 1a and 1b (Figures 6b and 7b). We generate this PDF using a slice sampling Monte Carlo Markov Chain approach (Neal, 2003) that samples the model space around Model 2a in a more complete way than the somewhat irregular sampling provided by the *binary* method, ultimately generating 1,000 models of long-term slip rates and slip deficit accumulation rates that yield 1,000 samples of the total moment deficit accumulation rate (supporting information Text S8; Minson et al., 2013; Neal, 2003). These 1,000 samples form a PDF that peaks at 1.3×10^{17} Nm/year (Figure 8b), comparable to the weighted mean rate of Model 2a.

5.3.1. Model 2b

Finally, as Model 2a allowed strain accumulation both west and east of the basin like Model 1a, we test the impact of relaxing this assumption while enforcing sharp creep-to-locking transitions by running the binary method on models that disallow strain accumulation east of the Los Angeles basin. Using the same log likelihood cutoff as Model 2a, we then combine these models into a unified estimate of long-term slip rates and the accumulation rates of slip deficit and moment deficit, yielding Model 2b of interseismic strain accumulation (Figure 9). As in the comparison of Models 1b and 1a, Model 2b fits the azimuths of velocities on the east side of the basin better than Model 2a (Figure 9a), offers an equally good overall fit to the data (X^2/N = 0.46), and infers a higher slip rate (5.0 mm/year) and higher slip deficit accumulation rates on the Sierra Madre Fault than Model 2a, again perhaps because this configuration disallows strain accumulation along the Cucamonga Fault to the east. The total moment deficit accumulation rate is therefore slightly higher in Model 2b, at 1.6×10^{17} Nm/year, and the corresponding PDF, constructed as above, also peaks at this value (Figure 9b). We use all four strain accumulation models and their PDFs in the subsequent analysis and discussion.

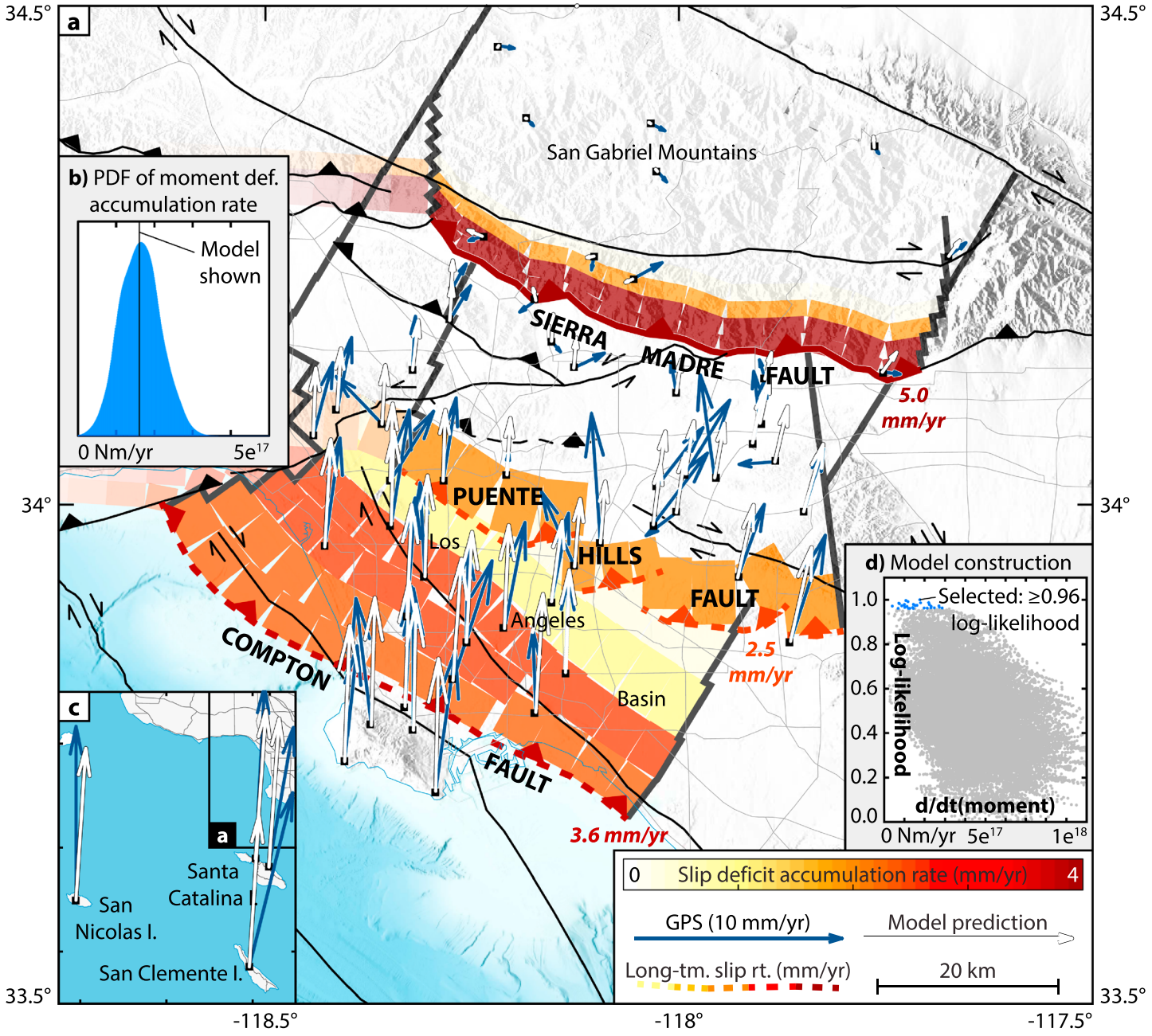

Figure 9. Model 2b of slip deficit accumulation rates and long-term slip rates, the weighted average of a set of binary creep/locking models disallowing strain accumulation east of the basin that have normalized log-likelihood ≥0.96. (a) Map view of slip deficit accumulation rates (colored patches), long-term slip rates (colors of the solid and dashed fault traces, also noted next to the faults), and observed (dark blue) and predicted (blue) velocities at GPS stations. (b) Corresponding PDF of moment deficit accumulation rate. (c) Comparison of observed and predicted velocities on islands. (b) Distribution of moment deficit accumulation rate versus normalized log likelihood in the set of binary models.

6. Implications of the Strain Accumulation Models

6.1. Depth Distributions of Moment Accumulation, Moment Release, and Seismicity

One of the motivations for this study was the discrepancy between the lower locking depths of 6 ± 2, ~8, and ~3 km in the interseismic strain accumulation models of Argus et al. (2005), Marshall et al. (2009), and Daout et al. (2016) and the observation that most seismicity in Los Angeles in fact occurs below those depths. The high-quality seismic catalogs available for Los Angeles allow us to evaluate the predictive power of our

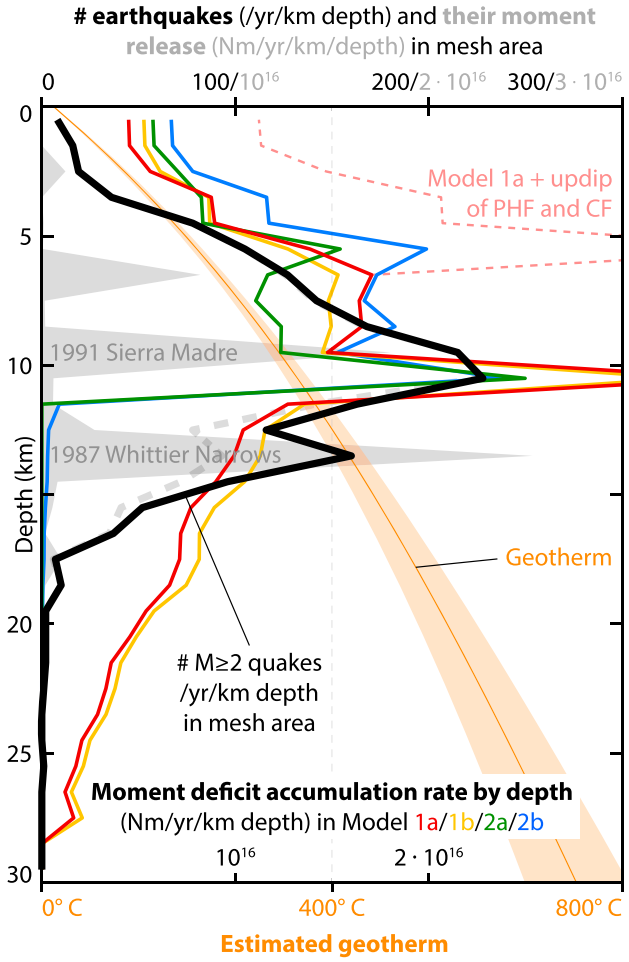

Figure 10. Depth distributions of moment deficit accumulation rate in the four strain accumulation models (red, yellow, green, and blue lines for Models 1a, 1b, 2a, and 2b, respectively) compared with the depth distribution of earthquake rates (black line) in the Hauksson et al. (2012 and updated) relocated catalog whose epicenters lie within in the mesh area of the thrust faults and decollement, as well as the depth distribution of moment release rate in the same earthquakes (gray shape). Orange PDF is an estimated geotherm (supporting information Text S9). The depth distribution of moment deficit accumulation in Model 1a would follow the dashed red line if all three faults extended to the surface. The depth distribution of earthquake rates would follow the dashed gray line if earthquakes whose epicenters lie within 10 km of the 1987 Whittier Narrows event, and which occurred in the 1-year period beginning with it, were excluded. PHF: Puente Hills Fault. CF: Compton Fault.

models with respect to earthquake production. Hauksson et al. (2012) relocated earthquakes from the Southern California Earthquake Data Center for the period 1981–2011 and have since updated their relocated catalog through 2016 (http://scedc.caltech.edu/research-tools/alt-2011-dd-hauksson-yang-shearer.html). We use the earthquakes in this updated catalog whose epicenters lie within the boundary of the mesh of the three thrust faults and decollement (Figure 3, white circles); we henceforth refer to this set as HYS16.

We first compare the depth distribution of seismic moment deficit accumulation rate in the four models with the depth distribution of seismic moment release in HYS16 (Figure 10). The latter is visibly dominated by the largest few earthquakes (Figure 10a, gray polygon), in particular the 1987 *Mw* ~ 5.9 Whittier Narrows and 1991 *Mw* ~ 5.8 Sierra Madre earthquakes. The Whittier Narrows earthquake occurred at ~13-km depth; Models 2a and 2b, by virtue of inferring no strain accumulation below ~11-km depth, imply that this earthquake, the largest in HYS16, should be rare over the long term. However, this comparison is subject to statistics of small numbers and is therefore of limited use.

We then compare the depth distribution of moment deficit accumulation rate in the four models to the depth distribution of earthquake rates in HYS16 (Figure 10a, black line). The two match to first order, both increasing downward to a maximum at ~11-km depth and decreasing below that. The match is unaffected if one excludes the Whittier Narrows earthquake and its aftershocks (Figure 10a, gray dashed line). Although slip deficit accrues fastest on the uppermost sections of faults in all four models, seismic moment accrues most quickly at depth in all four for two reasons. First, the shear modulus, which factors into moment deficit accumulation rate, increases with depth in the CVM* (Figure S9); thus, for example, the Sierra Madre accrues moment deficit most rapidly at ~6- to 9-km depth in Model 1a (Figure S11) despite accruing slip deficit most rapidly at the surface (Figure 6a). Second, the Puente Hills and Compton Faults only begin adding to the moment deficit accumulation rate at ~3- and ~5-km depths, respectively, as we assume that deformation updip of their tips occurs anelastically. For comparison, we derive a supplementary strain accumulation model from Model 1a in which we count the strain accumulation on the surface extensions that are used to represent the blind nature of these faults (5.1). This model produces a depth distribution of moment deficit accumulation rates (Figure 10, dashed red line) that is inconsistent with the decrease of seismicity toward the surface. The incorporation of the blind nature of the Puente Hills and Compton Faults into the models, all else being equal, thus appears to produce a more plausible result along these lines.

Below the peak at ~11-km depth, moment deficit accumulation rates decrease gradually with depth in Models 1a and 1b but are uniformly zero in Models 2a and 2b (Figure 10). The proportional decrease in earthquake rates in HYS16 below 11-km depth lies in between these two predictions. If seismic moment deficit accumulation rates and earthquake rates are usable proxies for one another by depth—as their similarity in shape at shallower depths suggests but does not prove—the implication would be that the true creep-to-locking transition at depth is sharper than in 1a and 1b but less sharp than in 2a and 2b.

6.2. Spatial Distribution and PDF of Seismic Moment Deficit Accumulation Rate

The models can also be used to construct a map of moment deficit accumulation rate per area in the Los Angeles basin (Figure 11a). At each point at the surface, we estimate this as the moment deficit

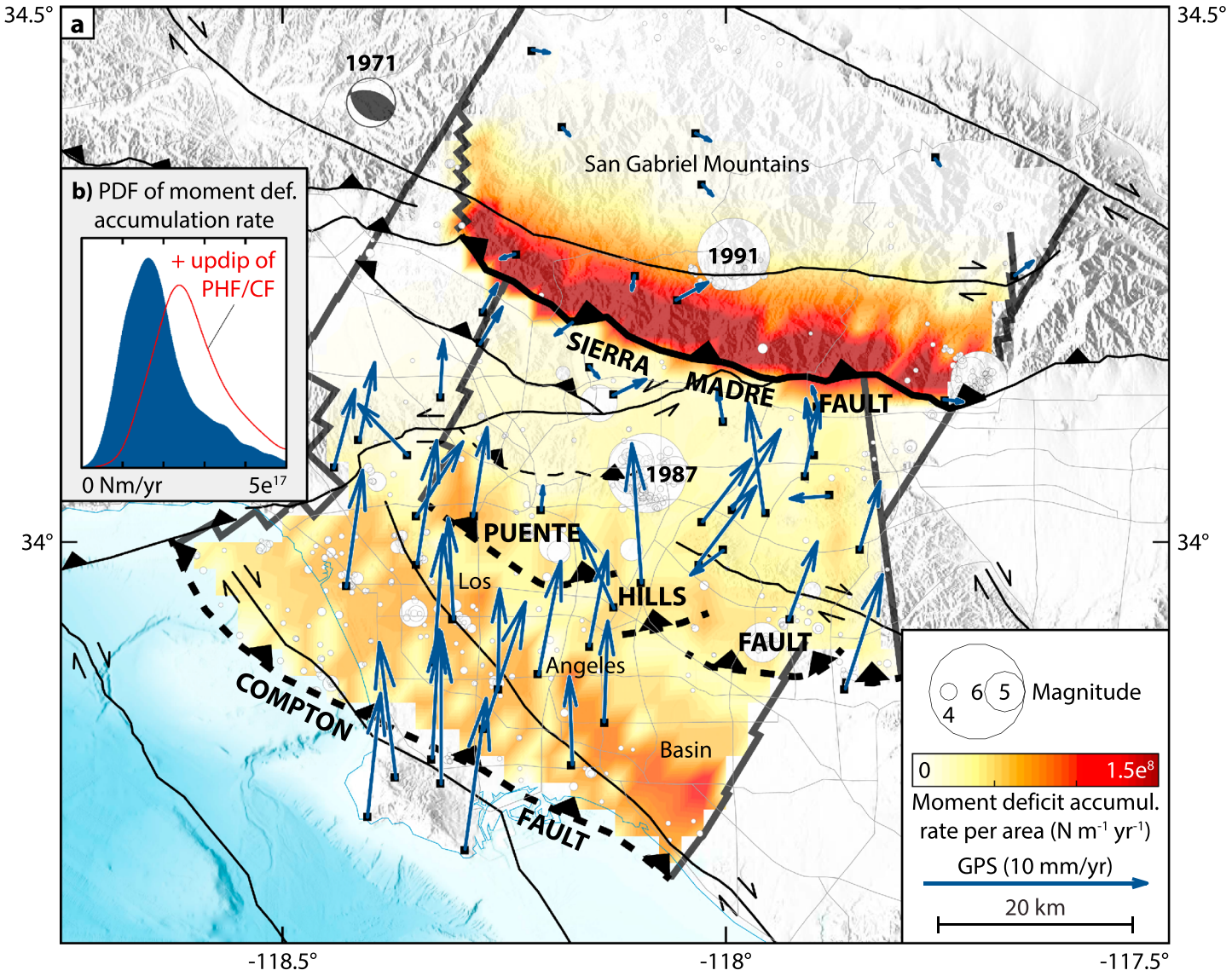

Figure 11. Estimates of moment deficit accumulation rate from combining the four interseismic strain accumulation models. (a) Spatial distribution of moment deficit accumulation rate per area. (Values are on the order of ~10^8 N m^{-1} yr^{-1} as the moment deficit accumulation rate per patch is on the order of 10^{15} N m^{-1} yr^{-1} [Figure S11] and the patches are a few kilometers (a few thousand meters) on a side.) (b) Unified PDF of moment deficit accumulation rate (dark blue object) formed by combining the PDFs from the four strain accumulation models. The PDF would follow the red curve if strain accumulation updip of the tips of the Puente Hills and Compton faults (PHF and CF) were counted.

accumulation rate on all of the portions of faults that underlie that point (per square meter) averaged between the four models. (An example using only Model 1a is shown in Figure S19; the corresponding 3-D distribution of moment deficit accumulation rate is shown in Figure S11). The highest values are found around the Sierra Madre Fault (Figure 11a), a result of two factors. The first is that all four models infer the fastest slip deficit accumulation rates in the system to be on the shallow portion of this fault. The second is that the Sierra Madre's steep northward dip means that a given horizontal two-dimensional area corresponds to a larger on-fault area, and therefore a faster moment deficit accumulation rate, than on the other two faults. The moment deficit accumulation rate per area is comparably moderate over the Puente Hills and Compton Faults (Figure 11a). Note that as the models incorporate strain accumulation west and in some cases east of the basin, they imply that seismic moment accumulation would not stop at the edges of the fault mesh. We only discuss moment deficit accumulation in the study area here as it is less well resolved outside the basin in our approach.

Finally, combining the PDFs of moment deficit accumulation rate from the four models, we estimate that seismic moment deficit is accruing on the three thrust faults at a cumulative rate of $1.6 + 1.3/-0.5 \times 10^{17}$ Nm/year (Figure 11b). (These are the mode and 16th and 84th percentiles of the unified PDF.) If strain accumulation on the updip extensions of the Puente Hills and Compton Faults were counted in all four models, the estimate would be $2.4 + 1.3/-0.6 \times 10^{17}$ Nm/year (Figure 11b, red line), ~50% faster.

7. Discussion

7.1. Effect of the Sedimentary Basin on the Estimation Problem

We find that the Los Angeles sedimentary basin amplifies elastostatic Green's functions from slip on faults underlying it by up to ~50% (Figure 4), consistent with the effects of near-surface material heterogeneity inferred in previous studies. In particular, Cattin et al. (1999) computed elastostatic Green's functions from slip on a dislocation in a substrate overlain by a weak near-surface layer and found that the amplification by the layer is ~50% when the layer is 2 orders of magnitude less stiff than the substrate, approximately the contrast in shear modulus between the Los Angeles basin and surrounding crust at the surface (Figure 1a). We find that the specific details of the basin model have very little effect on the computed Green's functions (Figure S4). This contrasts with their significant effect in simulations of seismic shaking (e.g., Taborda & Bielak, 2014) but is also consistent with the findings of Cattin et al. (1999), which showed in the aforementioned analysis that the amplification by the near-surface layer approaches 50% asymptotically with decreasing stiffness. We find that incorporating the CVM* into inversions for interseismic strain accumulation increases the inferred slip deficit accumulation rates and moment deficit accumulation rates on the faults at depth (Figures 6 and S11), consistent with previous work showing that incorporating elastic heterogeneity into models in which the fault underlies the relevant low-stiffness layer results in more inferred slip and seismic moment (Cattin et al., 1999).

7.2. Contribution of Strike-Slip Faults to the North-South Shortening

Walls et al. (1998) proposed that as much as half of the north-south shortening across Los Angeles could be the product of east-west escape tectonics on strike-slip faults; Argus et al. (1999) found, however, that this model overpredicted east-westsurface velocities in northern Los Angeles as compared to GPS data. Both studies modeled long-term slip rates on the faults rather than interseismic strain accumulation. Bawden et al. (2001) modeled interseismic strain accumulation on the major strike-slip faults assuming locking down to ~10-km depth and inferred that this could contribute ~0.7 mm/year of north-south contraction in addition to rotating the inferred azimuth of the shortening by ~20°. We note that the Bawden et al. model does not appear to include other model elements that we find are necessary to represent strain accumulation on confined faults in the back slip framework, such as steps in surface velocity over the faults and semiinfinite extensions along strike (supporting information Text S4). These elements may not drastically affect Bawden et al.'s conclusions on the scale of the basin, however. We use a forward-slip model to represent interseismic strain accumulation on the strike-slip faults, which may be more internally self-consistent, and find that this could be contributing ~1–2 mm/year of north-south contraction while producing relatively little east-west motion in the basin (Figures 5 and S7). The latter attribute contrasts with the finding of Argus et al. (1999); the difference may principally arise from our inclusion of shallow locking on the faults. The forward model where the strike-slip faults are locked down to ~5-km depth (Figure 5) would imply that most seismicity should be shallower than that, which is inconsistent with the HYS16 catalog (Figure 10); the model where they are locked down to ~13-km depth (Figure S7) is more consistent with the depth distribution of seismicity but predicts only ~1.1 mm/year of total north-south shortening. Because the strike-slip faults are near-vertical and contribute less total locked area of fault in the study area than the thrust faults, the total moment deficit accumulation rates in the study area in these two models are only 1.3×10^{16} and 6.0×10^{16} Nm/year, respectively, far less than any of the thrust models. In parallel, the accumulation rates of slip deficit and total moment deficit on the thrust faults change only slightly if the strike-slip faults are accounted for a priori (supporting information Text S6 and Figure S14a). In sum, the contribution of strike-slip faults to the interseismic shortening and total moment deficit accumulation rate is likely less than that of the thrust faults.

7.3. Contribution of Strain Accumulation West and East of the Los Angeles Basin

We find that models that incorporate strain accumulation west of the Los Angeles basin (e.g., Figures 6–9) offer a more convincing fit to first-order features of the GPS data than models that do not (Figure S15),

suggesting that strain accumulation to the west does influence the pattern of shortening in the basin. This is not surprising, as multiple extensive reverse faults are thought to accrue strain west of the Los Angeles basin (e.g., Dolan et al., 1995; Hager et al., 1999). By contrast, incorporating strain accumulation on north dipping thrust faults east of the basin does not improve the fit to the data (Figures 7a and 9a). This may reflect the decreased role of thrust faulting east of the basin with increasing proximity to the San Jacinto, Elsinore, and San Andreas faults. Thus, the geodetic shortening pattern in Los Angeles appears to be consistent with a transition from rapid reverse faulting on the west to strike-slip tectonics on the east.

7.4. Comparison With the Depth Distribution of Seismicity

The depth distribution of seismic moment accumulation in the four strain accumulation models reproduces the general characteristics of the depth distribution of earthquake rates in Los Angeles (Figure 10). This is not an unequivocal validation of the strain accumulation models; in particular, by counting all earthquakes in the HYS16 catalog that occur within the mesh area, we are comparing strain accumulation on three faults to earthquakes in the volume around the three faults, which may not be entirely rigorous. This correlation nevertheless suggests that the strain accumulation models are not indefensible (as would be implied if the moment deficit accumulation rates in all four were fastest at 25-km depth, for example).

Both seismicity rates and the inferred moment deficit accumulation rates decrease with depth below ~11-km depth (Figure 10), qualitatively reflecting the increasing contribution of steady-sliding behavior to fault rheology. This transition is commonly thought to depend primarily on temperature (e.g., Avouac, 2015). To evaluate this possibility here, we estimate a geotherm for the Los Angeles area (Figure 10, tan curve) using five measurements of temperature and heat flow in the eastern Los Angeles basin provided by the SMU Geothermal Data Aggregation (http://geothermal.smu.edu/gtda/). Details of the estimation are provided in supporting information Text S9 (Tanaka & Ishikawa, 2002). The peak of the depth distribution of seismicity and of seismic moment deficit accumulation rate in the four models corresponds to a temperature of ~350 °C in the estimated geotherm; this is consistent with laboratory measurements on quartzofeldspathic rocks that show a transition from rate-weakening (stick-slip) to rate-strengthening (creeping) behavior in the temperature range ~300–450 °C (e.g., Blanpied et al., 1991). This suggests that the general characteristics of the strain accumulation models may be plausible. Furthermore, the smoothed and binary inversion schemes were designed to test the alternate hypotheses that the creep-to-locking transition might be gradual (in the former case) or sharp (in the latter). If temperature is indeed the dominant control on fault rheology, the seismicity distributions predicted by these two alternate hypotheses should theoretically begin to differ around 300–450 °C (rather than at 100° or 700 °C, for example). This is indeed where the model predictions bifurcate (Figure 10), despite the fact that the models are based entirely on geodetic data.

7.5. Inferred Total Moment Deficit Accumulation Rate

The limited seismicity in the upper 5 km (Figure 10) suggests that deformation updip of the blind Puente Hills and Compton faults is likely mostly anelastic and aseismic. Under this assumption, we estimate that the total moment deficit accumulation rate is $1.6 + 1.3/-0.5 \times 10^{17}$ Nm/year (Figure 11b). If strain updip of the fault tips were in fact accommodated elastically and ought to be counted in the estimate of moment deficit accumulation, the total rate would be $2.4 + 1.3/-0.6 \times 10^{17}$ Nm/year, approximately 50% faster (Figure 11b, red line). Although this estimate excludes the contribution of strike-slip faults, it would likely be little changed if they were accounted for (7.2). Based on a regional scale geodetic inversion, Meade and Hager (2005b) estimated that seismic moment deficit is accumulating on two faults beneath greater Los Angeles at a rate equivalent to a $Mw = 7.0$ earthquake every 200 years on each fault. Only one of these sources is within the Los Angeles basin, corresponding to an estimated moment deficit accumulation rate within the basin of $\sim 2 \times 10^{17}$ Nm/year in total, close to our estimates. This agreement is perhaps surprising as the Meade and Hager study prescribed a uniform locking depth of 15 km on most faults and counted moment deficit accumulation up to the surface; however, the different inversion methodology and block geometries used in that study make quantitative comparisons difficult. This suggests nevertheless that our models may be reconcilable with more regional scale studies.

7.6. Comparison of Long-Term Slip Rates With Geologic and Paleoseismologic Estimates

All four strain accumulation models infer long-term slip rates of 4–5 mm/year on the Sierra Madre Fault, ~3 mm/year on the Puente Hills, and 3–4 mm/year on the Compton. These rates are higher than most

estimates from geologic and paleoseismologic studies, with the exception of the slip rate of 3.6–5.7 mm/year inferred on the western Sierra Madre Fault by Meigs et al. (2003). On the Sierra Madre Fault, Walls et al. (1998) estimated a slip rate of 1–2 mm/year on the western section, Tucker and Dolan (2001) estimated a slip rate of 0.6–0.9 mm/year on the central section, and Rubin et al. (1998) inferred ~11 m of total displacement in two paleoearthquakes since ~15 ka, translating into an average slip rate of ~0.6 mm/year (Glasscoe et al., 2004). On the Puente Hills Fault, Bergen et al. (2017) inferred a recent slip rate of 1.33 + 0.4/−0.2 mm/year on the Los Angeles segment, Leon et al. (2009) and Myers et al. (2003), respectively, inferred slip rates of 1.1–1.6 mm/year (1.4–2.4 mm/year in an alternate estimate) and 1.5 mm/year on the Santa Fe Springs segment, and Shaw et al. (2002) and Myers et al. (2003), respectively, inferred slip rates of 1.28 and 1.5 mm/year on the Coyote Hills segment. On the Compton Fault, Shaw and Suppe (1996) and Leon et al. (2009), respectively, inferred slip rates of 1.2 and 1.4 mm/year, although the latter study speculated that the true rate could be as high as ~2 mm/year as per geometrical arguments. Individually, our models can likely be brought into approximate agreement with the latter rates on the Compton if the possible contribution from strike-slip faults (in particular the Palos Verdes Fault) is accounted for a priori and if velocities on islands are excluded (supporting information Text S6 and Figure S14).

Nevertheless, our estimated long-term slip rates still exceed most values from geologic and paleoseismologic studies. It is worth discussing several factors that could lead to this discrepancy, as they may indeed apply both in Los Angeles and elsewhere. First, geologic and paleoseismologic estimates of slip rates on blind thrust faults are constructed based on models of long-term anelastic fault-bend and fault-tip folding (e.g., Leon et al., 2007, 2009; Shaw & Suppe, 1996). While our preferred models assume that deformation updip of the blind thrust faults is anelastic, they are based on interseismic data and do not specify the nature of this anelastic deformation, potentially leading to different interpretations. This argument would not apply along the Sierra Madre Fault, however.

Second, anelastic deformation of the medium could be accommodating some of the north-south shortening. Abundant evidence for off-fault pressure solution creep, for example, has been found in the nearby Ventura basin (Deubendorfer et al., 1998). Sedimentary structures overlying the Compton Fault are cleanly discernable in reflection profiles (Shaw & Suppe, 1996), suggesting that off-fault anelastic deformation may be less prevalent in the Los Angeles basin; nonetheless, it may play some role in absorbing strain.

Third, some of the shortening could be accommodated along faults not modeled here. The Sierra Madre Fault has multiple strands: the Clamshell-Sawpit strand produced the 1991 Sierra Madre earthquake (Hauksson, 1994) and the 1971 San Fernando earthquake may have ruptured two north-dipping strands (Heaton, 1982). Smaller faults may also contribute, such as the Upper Elysian Park, Verdugo, San Vicente, Walnut Creek, East Montebello Hills, Workman Hill, and Peralta Hills faults (e.g., Marshall et al., 2009), and structures such as a back thrust above the Puente Hills Fault inferred by Shaw et al. (2002) and a multiple-layer thrust system inferred in Palos Verdes by Sorlien et al. (2013).

Another hypothesis is that the north-south shortening could have itself recently accelerated, perhaps due to regional geodynamic processes (Dolan et al., 2007), prolonged changes in fault behavior (e.g., due to stress changes from earthquakes), or temporal variations in strain partitioning processes. As the paleoseismologic studies include events within the last 3 ka (Leon et al., 2007, 2009), such an acceleration would need to have occurred comparably recently in order for present-day slip rates to significantly exceed the paleoseismologic rates. If earthquake production scales positively with strain rate (e.g., Kreemer et al., 2014), such an acceleration should presumably have driven a recent increase in earthquake rates; however, paleoearthquakes have in fact apparently been infrequent in Los Angeles over the past millennium compared to Holocene averages (Dolan et al., 2007). It should nevertheless be noted that our models implicitly assume that all deformation rates are constant through time. Slip rates have in fact likely varied over geologic time on at least two segments of the Puente Hills Fault (Bergen et al., 2017; Myers et al., 2003). Although these variations are over much longer timescales than the late Holocene acceleration speculated above and do not help to reconcile the geologic and geodetic slip rates in this case, they illustrate that such temporal variations may affect this comparison in other settings.

Another hypothesis is that postseismic deformation from past earthquakes could be affecting the interseismic velocity field (e.g., Hager et al., 1999). However, Argus et al. (2005) found no evidence for postseismic deformation following the 1994 Northridge earthquake in geodetic data when preparing the velocity field

used here, and Glasscoe et al. (2004) showed that postseismic deformation is unlikely to affect surface velocities in Los Angeles for more than a few years under realistic parametrizations, meaning that earthquakes preceding Northridge are likely to have much effect on present-day geodetic velocities either. The 1857 *Mw* ~ 7.9 Fort Tejon earthquake could have triggered widespread and long-lasting postseismic deformation, but as shown for that case by Hearn et al. (2013) and for a thrust setting by Hager et al. (1999), such deformation should cause present-day geodetic deformation rates to trail average rates not substantially exceed geologic and paleoseismologic rates. Meade and Hager (2005a) and Argus et al. (2005) also found no evidence for region-wide postseismic deformation in southern California at present day.

Finally, it should also be noted that our models assume that the long-term slip rates on the faults are essentially uniform along strike, as the motion of the intervening blocks is a rotation about a global Euler pole and is nearly uniform in velocity and azimuth across the study sarea (Figure S2). In reality, inferred long-term slip rates are inferred to vary from west to east along at least the Puente Hills and Sierra Madre faults (e.g., Shaw et al., 2002; Tucker & Dolan, 2001). Denser geodetic coverage of the north-south shortening, corrected for anthropogenic motions, may invite more intricate models of long-term block motion and interseismic strain accumulation. The considerations discussed in this study may nonetheless prove useful in such analyses.

8. Conclusion

We characterize the ways in which the ~8.5 mm/year of north-south shortening inferred across Los Angeles in geodetic data may be accommodated by interseismic strain accumulation on subsurface faults. Using a computationally efficient method to compute high-resolution elastostatic Green's functions, we find that the elastic heterogeneity due to the sedimentary fill of the Los Angeles basin has a nonnegligible effect on this estimation problem and that strain accumulation on strike-slip faults—the contribution of which has been previously debated in the literature—may contribute ~1–2 mm/year of the shortening but likely no more. We develop four complementary models of interseismic strain accumulation on the Sierra Madre, Puente Hills, and Compton Faults that examine a wide range of model assumptions. The four models feature long-term slip rates of 4–5, ~3, and 3–4 mm/year on the Sierra Madre, Puente Hills, and Compton faults, respectively, and infer that interseismic strain is accruing on (at least) the upper sections of the faults at present day. These models predict depth distributions of seismic moment deficit accumulation rate that match the depth distribution of earthquake rates in the study area to first order, in part, because the Puente Hills and Compton faults are modeled as blind; the interpretation of strain accumulation in the middle and lower crust is subject to whether the transition from stick slip to steady sliding is assumed to be gradual or sharp. Using the four strain accumulation models, we estimate that seismic moment is accumulating on the Sierra Madre, Puente Hills, and Compton faults at a rate of $1.6 + 1.3/-0.5 \times 10^{17}$ Nm/year. This total rate would likely be little changed if locking on strike-slip faults were accounted for. This estimate, the four models, and the various tools can be used in future studies of seismic hazard and fault behavior in this region and elsewhere.

Acknowledgments

C. Rollins was supported by the NASA Earth and Space Science Fellowship for the duration of this work. The authors are grateful to Scott T. Marshall and two anonymous reviewers for suggestions that greatly improved the manuscript, as well as numerous colleagues around the community for helpful input and guidance. The authors declare no competing financial interests. The GPS data used here can be found in Argus et al. (2005), Table 3; the *HYS16* seismic catalog is available at http://scedc.caltech.edu/research-tools/alt-2011-dd-hauksson-yang-shearer.html.

References

Ader, T., Avouac, J.-P., Liu-Zeng, J., Lyon-Caen, H., Bollinger, L., Galetzka, J., et al. (2012). Convergence rate across the Nepal Himalaya and interseismic coupling on the Main Himalayan Thrust: Implications for seismic hazard. *Journal of Geophysical Research*, *117*, B04403. https://doi.org/10.1029/2011JB009071

Allmendinger, R. W., & Shaw, J. H. (2000). Estimation of fault propagation distance from fold shape: Implications for earthquake hazard assessment. *Geology*, *28*(12), 1099–1102.

Argus, D. F., & Gordon, R. G. (2001). Present tectonic motion across the Coast Ranges and San Andreas fault system in central California. *Geological Society of America Bulletin*, *113*(12), 1580–1592.

Argus, D. F., Heflin, M. B., Donnellan, A., Webb, F. H., Dong, D., Hurst, K. J., et al. (1999). Shortening and thickening of metropolitan Los Angeles measured and inferred by using geodesy. *Geology*, *27*(8), 703–706.

Argus, D. F., Heflin, M. B., Peltzer, G., Crampé, F., & Webb, F. H. (2005). Interseismic strain accumulation and anthropogenic motion in metropolitan Los Angeles. *Journal of Geophysical Research*, *110*, B04401. https://doi.org/10.1029/2003JB002934

Arnadottir, T., & Segall, P. (1991). A fault model for the 1989 Kilauea south flank earthquake from leveling and seismic data. *Geophysical Research Letters*, *18*(12), 2217–2220.

Aster, R., Borchers, B., & Thurber, C. (2012). *Parameter estimation and inverse problems*. Waltham, MA: Academic Press.

Avouac, J.-P. (2015). From geodetic imaging of seismic and aseismic fault slip to dynamic modeling of the seismic cycle. *Annual Review of Earth and Planetary Sciences*, *43*, 233–271.

Barbot, S., Agram, P., & De Michele, M. (2013). Change of apparent segmentation of the San Andreas fault around Parkfield from space geodetic observations across multiple periods. *Journal of Geophysical Research: Solid Earth*, *118*, 6311–6327. https://doi.org/10.1002/2013JB010442

Bawden, G. W., Thatcher, W., Stein, R. S., Hudnut, K. W., & Peltzer, G. (2001). Tectonic contraction across Los Angeles after removal of groundwater pumping effects. *Nature*, *412*(6849), 812–815.

Bergen, K. J., Shaw, J. H., Leon, L. A., Dolan, J. F., Pratt, T. L., Ponti, D. J., et al. (2017). Accelerating slip rates on the Puente Hills blind thrust fault system beneath metropolitan Los Angeles, California, USA. *Geology*, *45*(3), 227–230.
Bernard, P., Briole, P., Meyer, B., Lyon-Caen, H., Gomez, J.-M., Tiberi, C., et al. (1997). The Ms = 6.2, June 15, 1995 Aigion earthquake (Greece): Evidence for low angle normal faulting in the Corinth rift. *Journal of Seismology*, *1*(2), 131–150.
Blanpied, M., Lockner, D., & Byerlee, J. (1991). Fault stability inferred from granite sliding experiments at hydrothermal conditions. *Geophysical Research Letters*, *18*(4), 609–612.
Blythe, A., Burbank, D., Farley, K., & Fielding, E. (2000). Structural and topographic evolution of the central Transverse Ranges, California, from apatite fissiontrack, (U–Th)/He and digital elevation model analyses. *Basin Research*, *12*(2), 97–114.
Broderick, K. G. (2006). *Giant blind thrust faults beneath the Palos Verdes Hills and western Los Angeles Basin, California: Mapping with seismic reflection and deep drilling data*. (MS thesis, Department of Earth Science, University of California, Santa Barbara, Santa Barbara, CA).
Brune, J. N. (1968). Seismic moment, seismicity, and rate of slip along major fault zones. *Journal of Geophysical Research*, *73*(2), 777–784.
Bürgmann, R., Kogan, M. G., Steblov, G. M., Hilley, G., Levin, V. E., & Apel, E. (2005). Interseismic coupling and asperity distribution along the Kamchatka subduction zone. *Journal of Geophysical Research*, *110*, B07405. https://doi.org/10.1029/2005JB003648
Cattin, R., Briole, P., Lyon-Caen, H., Bernard, P., & Pinettes, P. (1999). Effects of superficial layers on coseismic displacements for a dip-slip fault and geophysical implications. *Geophysical Journal International*, *137*(1), 149–158.
Chlieh, M., Avouac, J.-P., Sieh, K., Natawidjaja, D. H., & Galetzka, J. (2008). Heterogeneous coupling of the Sumatran megathrust constrained by geodetic and paleogeodetic measurements. *Journal of Geophysical Research*, *113*, B05305. https://doi.org/10.1029/2007JB004981
Chlieh, M., Perfettini, H., Tavera, H., Avouac, J.-P., Remy, D., Nocquet, J. M., et al. (2011). Interseismic coupling and seismic potential along the Central Andes subduction zone. *Journal of Geophysical Research*, *116*, B12405. https://doi.org/10.1029/2010JB008166
Cooke, M. L., & Marshall, S. T. (2006). Fault slip rates from three-dimensional models of the Los Angeles metropolitan area, California. *Geophysical Research Letters*, *33*, L21313. https://doi.org/10.1029/2006GL027850
Daout, S., Barbot, S., Peltzer, G., Doin, M.-P., Liu, Z., & Jolivet, R. (2016). Constraining the kinematics of metropolitan Los Angeles faults with a slip-partitioning model. *Geophysical Research Letters*, *43*, 11,192–11,201. https://doi.org/10.1002/2016GL071061
Davis, T. L., Namson, J., & Yerkes, R. F. (1989). A cross section of the Los Angeles area: Seismically active fold and thrust belt, the 1987 Whittier Narrows earthquake, and earthquake hazard. *Journal of Geophysical Research*, *94*(B7), 9644–9664.
Dolan, J. F., Bowman, D. D., & Sammis, C. G. (2007). Long-range and long-term fault interactions in Southern California. *Geology*, *35*(9), 855–858. https://doi.org/10.1130/G23789A.1
Dolan, J. F., Christofferson, S. A., & Shaw, J. H. (2003). Recognition of paleoearthquakes on the Puente Hills blind thrust fault, California. *Science*, *300*(5616), 115–118.
Dolan, J. F., Sieh, K., Rockwell, T. K., Yeats, R. S., Shaw, J., Suppe, J., et al. (1995). Prospects for larger or more frequent earthquakes in the Los Angeles metropolitan region. *Science*, *267*(5195), 199–205.
Donnellan, A., Blythe, A., Kellogg, L., & Glasscoe, M. (2001). Strain partitioning across Metropolitan Los Angeles. *ACES Coop. for Earthquake Simulation, 2nd Workshop Proceedings*.
Donnellan, A., Hager, B. H., King, R. W., & Herring, T. A. (1993). Geodetic measurement of deformation in the Ventura Basin region, southern California. *Journal of Geophysical Research*, *98*(B12), 21,727–21,739.
Duebendorfer, E. M., Vermilye, J., Geiser, P. A., & Davis, T. L. (1998). Evidence for aseismic deformation in the western transverse ranges, southern California: Implications for seismic risk assessment. *Geology*, *26*(3), 271–274.
Elliott, J., Jolivet, R., González, P., Avouac, J.-P., Hollingsworth, J., Searle, M., & Stevens, V. (2016). Himalayan megathrust geometry and relation to topography revealed by the Gorkha earthquake. *Nature Geoscience*, *9*(2), 174–180.
Feigl, K. L., Agnew, D. C., Bock, Y., Dong, D., Donnellan, A., Hager, B. H., et al. (1993). Space geodetic measurement of crustal deformation in central and southern California, 1984–1992. *Journal of Geophysical Research*, *98*(B12), 21,677–21,712.
Field, E. H., Arrowsmith, R. J., Biasi, G. P., Bird, P., Dawson, T. E., Felzer, K. R., et al. (2014). Uniform California earthquake rupture forecast, version 3 (UCERF3)—The time-independent model. *Bulletin of the Seismological Society of America*, *104*(3), 1122–1180.
Fuis, G., Ryberg, T., Godfrey, N., Okaya, D., & Murphy, J. (2001). Crustal structure and tectonics from the Los Angeles basin to the Mojave Desert, southern California. *Geology*, *29*(1), 15–18.
Fuis, G. S., Scheirer, D. S., Langenheim, V. E., & Kohler, M. D. (2012). A new perspective on the geometry of the San Andreas fault in southern California and its relationship to lithospheric structure. *Bulletin of the Seismological Society of America*, *102*(1), 236–251.
Glasscoe, M. T., Donnellan, A., Kellogg, L. H., & Lyzenga, G. A. (2004). Evidence of strain partitioning between the Sierra Madre fault and the Los Angeles Basin, southern California from numerical models. *Pure and Applied Geophysics*, *161*(11–12), 2343–2357.
Godfrey, N. J., Fuis, G. S., Langenheim, V., Okaya, D. A., & Brocher, T. M. (2002). Lower crustal deformation beneath the central Transverse Ranges, Southern California: Results from the Los Angeles region seismic experiment. *Journal of Geophysical Research*, *107*(B7), 2144. https://doi.org/10.1029/2001JB000354
Hadley, D., & Kanamori, H. (1978). Recent seismicity in the San Fernando region and tectonics in the west-central Transverse Ranges, California. *Bulletin of the Seismological Society of America*, *68*(5), 1449–1457.
Hager, B. H., Lyzenga, G. A., Donnelan, A., & Dong, D. (1999). Reconciling rapid strain accumulation with deep seismogenic fault planes in the Ventura basin, California. *Journal of Geophysical Research*, *104*(B11), 25,207–25,219.
Hauksson, E. (1990). Earthquakes, faulting, and stress in the Los Angeles basin. *Journal of Geophysical Research*, *95*(B10), 15,365–15,394.
Hauksson, E. (1994). The 1991 Sierra Madre earthquake sequence in southern California: Seismological and tectonic analysis. *Bulletin of the Seismological Society of America*, *84*(4), 1058–1074.
Hauksson, E., Yang, W., & Shearer, P. M. (2012). Waveform relocated earthquake catalog for southern California (1981 to June 2011). *Bulletin of the Seismological Society of America*, *102*(5), 2239–2244.
Hearn, E., Pollitz, F., Thatcher, W., & Onishi, C. (2013). How do "ghost transients" from past earthquakes affect GPS slip rate estimates on southern California faults? *Geochemistry, Geophysics, Geosystems*, *14*, 828–838. https://doi.org/10.1002/ggge.20080
Heaton, T. H. (1982). The 1971 San Fernando earthquake: A double event? *Bulletin of the Seismological Society of America*, *72*(6A), 2037–2062.
Humphreys, E. D., & Hager, B. H. (1990). A kinematic model for the late Cenozoic development of southern California crust and upper mantle. *Journal of Geophysical Research*, *95*(B12). 19,747–19,762.
Kreemer, C., Blewitt, G., & Klein, E. C. (2014). A geodetic plate motion and Global Strain Rate Model. *Geochemistry, Geophysics, Geosystems*, *15*, 3849–3889. https://doi.org/10.1002/2014GC005407
Kositsky, A., & Avouac, J. P. (2010). Inverting geodetic time series with a principal component analysis-based inversion method. *Journal of Geophysical Research*, *115*, B03401. https://doi.org/10.1029/2009JB006535
Landry, W., & Barbot, S. (2016). Gamra: Simple meshing for complex earthquakes. *Computers & Geosciences*, *90*, 49–63.
Lekic, V., French, S. W., & Fischer, K. M. (2011). Lithospheric thinning beneath rifted regions of Southern California. *Science*, *334*(6057), 783–787.

Leon, L. A., Christofferson, S. A., Dolan, J. F., Shaw, J. H., & Pratt, T. L. (2007). Earthquake-by-earthquake fold growth above the Puente Hills blind thrust fault, Los Angeles, California: Implications for fold kinematics and seismic hazard. *Journal of Geophysical Research*, *112*, B03S03. https://doi.org/10.1029/2006JB004461

Leon, L. A., Dolan, J. F., Shaw, J. H., & Pratt, T. L. (2009). Evidence for large Holocene earthquakes on the Compton thrust fault, Los Angeles, California. *Journal of Geophysical Research*, *114*, B12305. https://doi.org/10.1029/2008JB006129

Leveque, R. J., & Li, Z. (1994). The immersed interface method for elliptic equations with discontinuous coefficients and singular sources. *SIAM Journal on Numerical Analysis*, *31*(4), 1019–1044.

Li, Y. G. (1996). Shear wave splitting observations and implications on stress regimes in the Los Angeles basin, California. *Journal of Geophysical Research*, *101*(B6), 13,947–13,961.

Lisowski, M., Savage, J., & Prescott, W. (1991). The velocity field along the San Andreas fault in central and southern California. *Journal of Geophysical Research*, *96*(B5), 8369–8389.

Marshall, S. T., Cooke, M. L., & Owen, S. E. (2009). Interseismic deformation associated with three-dimensional faults in the greater Los Angeles region, California. *Journal of Geophysical Research*, *114*, B12403. https://doi.org/10.1029/2009JB006439

Marshall, S. T., Funning, G. J., Krueger, H. E., Owen, S. E., & Loveless, J. P. (2017). Mechanical models favor a ramp geometry for the Ventura-Pitas Point Fault, California. *Geophysical Research Letters*, *44*, 1311–1319. https://doi.org/10.1002/2016GL072289

Marshall, S. T., Funning, G. J., & Owen, S. E. (2013). Fault slip rates and interseismic deformation in the western Transverse Ranges, California. *Journal of Geophysical Research: Solid Earth*, *118*, 4511–4534. https://doi.org/10.1002/jgrb.50312

Marshall, S. T., & Morris, A. C. (2012). Mechanics, slip behavior, and seismic potential of corrugated dip-slip faults. *Journal of Geophysical Research*, *117*, B03403. https://doi.org/10.1029/2011JB008642

Matsu'ura, M., Jackson, D. D., & Cheng, A. (1986). Dislocation model for aseismic crustal deformation at Hollister, California. *Journal of Geophysical Research*, *91*(B12), 12,661–12,674.

Meade, B. J., & Hager, B. H. (2005a). Block models of crustal motion in southern California constrained by GPS measurements. *Journal of Geophysical Research*, *110*, B03403. https://doi.org/10.1029/2004JB003209

Meade, B. J., & Hager, B. H. (2005b). Spatial localization of moment deficits in southern California. *Journal of Geophysical Research*, *110*, B04402. https://doi.org/10.1029/2004JB003331

Meigs, A., Yule, D., Blythe, A., & Burbank, D. (2003). Implications of distributed crustal deformation for exhumation in a portion of a trans-pressional plate boundary, western Transverse ranges, southern California. *Quaternary International*, *101*, 169–177.

Meigs, A. J., Cooke, M. L., & Marshall, S. T. (2008). Using vertical rock uplift patterns to constrain the three-dimensional fault configuration in the Los Angeles Basin. *Bulletin of the Seismological Society of America*, *98*(1), 106–123.

Minson, S., Simons, M., & Beck, J. (2013). Bayesian inversion for finite fault earthquake source models I—Theory and algorithm. *Geophysical Journal International*, *194*(3), 1701–1726.

Molnar, P. (1979). Earthquake recurrence intervals and plate tectonics. *Bulletin of the Seismological Society of America*, *69*(1), 115–133.

Morton, D. M., & Matti, J. C. (1987). The Cucamonga fault zone: Geological setting and Quaternary history. *US Geological Survey Professional Paper*, *1339*, 179–203.

Myers, D. J., Nabelek, J. L., & Yeats, R. S. (2003). Dislocation modeling of blind thrusts in the eastern Los Angeles basin, California. *Journal of Geophysical Research*, *108*(B9), 2443. https://doi.org/10.1029/2002JB002150

Neal, R. M. (2003). Slice sampling. *Annals of Statistics*, *31*(3), 705–741.

Okada, Y. (1985). Surface deformation due to shear and tensile faults in a half-space. *Bulletin of the Seismological Society of America*, *75*(4), 1135–1154.

Ortega, F. (2013). Aseismic deformation in subduction megathrusts: Central Andes and North-East Japan. Ph.D. thesis, California Institute of Technology.

Oskin, M., Sieh, K., Rockwell, T., Miller, G., Guptill, P., Curtis, M., et al. (2000). Active parasitic folds on the Elysian Park anticline: Implications for seismic hazard in central Los Angeles, California. *Geological Society of America Bulletin*, *112*, 693–707.

Plesch, A., Shaw, J. H., Benson, C., Bryant, W. A., Carena, S., Cooke, M., et al. (2007). Community fault model (CFM) for southern California. *Bulletin of the Seismological Society of America*, *97*(6), 1793–1802.

Rollins, C. (2017). Using heterogeneous 3D Earth models to constrain interseismic and postseismic deformation in Southern California and Nepal. Ph.D. Thesis, California Institute of Technology.

Rubin, C. M., Lindvall, S. C., & Rockwell, T. K. (1998). Evidence for large earthquakes in metropolitan Los Angeles. *Science*, *281*(5375), 398–402.

Ryberg, T., & Fuis, G. S. (1998). The San Gabriel Mountains bright reflective zone: Possible evidence of young mid-crustal thrust faulting in southern California. *Tectonophysics*, *286*(1), 31–46.

Savage, J. (1983). A dislocation model of strain accumulation and release at a subduction zone. *Journal of Geophysical Research*, *88*(B6), 4984–4996.

Shaw, J. H., Plesch, A., Dolan, J. F., Pratt, T. L., & Fiore, P. (2002). Puente Hills blind-thrust system, Los Angeles, California. *Bulletin of the Seismological Society of America*, *92*(8), 2946–2960.

Shaw, J. H., Plesch, A., Tape, C., Suess, M. P., Jordan, T. H., Ely, G., et al. (2015). Unified structural representation of the southern California crust and upper mantle. *Earth and Planetary Science Letters*, *415*, 1–15.

Shaw, J. H., & Shearer, P. M. (1999). An elusive blind-thrust fault beneath metropolitan Los Angeles. *Science*, *283*(5407), 1516–1518.

Shaw, J. H., & Suppe, J. (1996). Earthquake hazards of active blind-thrust faults under the central Los Angeles basin, California. *Journal of Geophysical Research*, *101*(B4), 8623–8642.

Shen, Z. K., Jackson, D. D., & Ge, B. X. (1996). Crustal deformation across and beyond the Los Angeles basin from geodetic measurements. *Journal of Geophysical Research*, *101*(B12), 27,957–27,980.

Sorlien, C. C., Seeber, L., Broderick, K. G., Luyendyk, B. P., Fisher, M. A., Sliter, R. W., & Normark, W. R. (2013). The Palos Verdes anticlinorium along the Los Angeles, California coast: Implications for underlying thrust faulting. *Geochemistry, Geophysics, Geosystems*, *14*, 1866–1890. https://doi.org/10.1002/ggge.20112

Süss, M. P., & Shaw, J. H. (2003). P wave seismic velocity structure derived from sonic logs and industry reflection data in the Los Angeles basin, California. *Journal of Geophysical Research*, *108*(B3), 2170. https://doi.org/10.1029/2001JB001628

Taborda, R., & Bielak, J. (2014). Ground-motion simulation and validation of the 2008 Chino Hills, California, earthquake using different velocity models. *Bulletin of the Seismological Society of America*, *104*(4), 1876–1898. https://doi.org/10.1785/0120130266

Tanaka, A., & Ishikawa, Y. (2002). Temperature distribution and focal depth in the crust of the northeastern Japan. *Earth, Planets and Space*, *54*(11), 1109–1113.

Tape, C., Musé, P., Simons, M., Dong, D., & Webb, F. (2009). Multiscale estimation of GPS velocity fields. *Geophysical Journal International*, *179*(2), 945–971.

Tichelaar, B. W., & Ruff, L. J. (1989). How good are our best models? Jackknifing, bootstrapping, and earthquake depth. *Eos, Transactions of the American Geophysical Union*, *70*(20), 593–606.

Tucker, A. Z., & Dolan, J. F. (2001). Paleoseismologic evidence for a >8 ka age of the most recent surface rupture on the eastern Sierra Madre fault, northern Los Angeles metropolitan region, California. *Bulletin of the Seismological Society of America*, *91*(2), 232–249.

Walls, C., Rockwell, T., Mueller, K., Bock, Y., Williams, S., Pfanner, J., et al. (1998). Escape tectonics in the Los Angeles metropolitan region and implications for seismic risk. *Nature*, *394*(6691), 356–360.

Wright, T. L. (1991). Structural geology and tectonic evolution of the Los Angeles basin, California. *Active Margin Basins*, *52*, 35–134.

Yang, W., & Hauksson, E. (2013). The tectonic crustal stress field and style of faulting along the Pacific North America Plate boundary in Southern California. *Geophysical Journal International*, *194*, 100–117.

Yeats, R. S. (2004). Tectonics of the San Gabriel Basin and surroundings, southern California. *Geological Society of America Bulletin*, *116*(9–10), 1158–1182.

Zoback, M., Zoback, M., Eaton, J., Mount, V., & Suppe, J. (1987). New evidence on the state of stress of the San Andreas fault system. *Science*, *238*(4830), 1105–1111.